



HAL
open science

The structural landscape and diversity of *Pyricularia oryzae* MAX effectors revisited

Mounia Lahfa, Philippe Barthe, Karine De Guillen, Stella Cesari, Mouna Raji, Thomas Kroj, Marie Le Naour–Vernet, François Hoh, Pierre Gladieux, Christian Roumestand, et al.

► **To cite this version:**

Mounia Lahfa, Philippe Barthe, Karine De Guillen, Stella Cesari, Mouna Raji, et al.. The structural landscape and diversity of *Pyricularia oryzae* MAX effectors revisited. 2023. hal-04236508

HAL Id: hal-04236508

<https://hal.inrae.fr/hal-04236508v1>

Preprint submitted on 11 Oct 2023

HAL is a multi-disciplinary open access archive for the deposit and dissemination of scientific research documents, whether they are published or not. The documents may come from teaching and research institutions in France or abroad, or from public or private research centers.

L'archive ouverte pluridisciplinaire **HAL**, est destinée au dépôt et à la diffusion de documents scientifiques de niveau recherche, publiés ou non, émanant des établissements d'enseignement et de recherche français ou étrangers, des laboratoires publics ou privés.

1 **The structural landscape and diversity of *Pyricularia***
2 ***oryzae* MAX effectors revisited**

3
4 Mounia LAHFA¹, Philippe BARTHE¹, Karine DE GUILLEN¹, Stella CESARI², Mouna
5 RAJI¹, Thomas KROJ², Marie Le Naour--Vernet², François Hoh¹, Pierre GLADIEUX²,
6 Christian ROUMESTAND¹, Jérôme GRACY¹, Nathalie DECLERCK¹, André
7 PADILLA^{1*}

8
9 ¹ Centre de Biologie Structurale, Univ Montpellier, CNRS UMR 5048, INSERM U
10 1054, Montpellier, France.

11 ² PHIM Plant Health Institute, Univ Montpellier, INRAE, CIRAD, Institut Agro, IRD,
12 Montpellier, France

13
14 * Corresponding author

15 E-mail: andre.padilla@cbs.cnrs.fr

16
17 Keywords: *Pyricularia oryzae*, MAX effectors, NMR, protein structure, AlphaFold

18
19 Short title: MAX structural family portrait

20 **ABSTRACT**

21 Plant pathogenic fungi secrete a wide variety of small proteins, named
22 effectors. *Magnaporthe* AVR_s and ToxB-like (MAX) effectors constitute a superfamily
23 of secreted proteins widely distributed in *Pyricularia* (*syn. Magnaporthe*) *oryzae*, a
24 devastating fungus responsible for blast disease in cereals such as rice. In spite of
25 high evolutionary sequence divergence, MAX effectors share a common fold
26 characterized by a β -sandwich core often stabilized by a conserved disulfide bond.
27 In this study, we investigated the structural landscape and diversity within this
28 effector family based on a previous phylogenetic analysis of *P. oryzae* protein
29 sequences that identified 94 ortholog groups (OG) of putative MAX effectors.
30 Combining protein structure modeling approaches and experimental structure
31 determination, we validated the prediction of the conserved MAX core domain for 77
32 OG clusters. Four novel MAX effector structures determined by NMR were in
33 remarkably good agreement with AlphaFold2 (AF) predictions. Based on the
34 comparison of the AF-generated 3D models we propose an updated classification of
35 the MAX effectors superfamily in 20 structural groups that highlight variation
36 observed in the canonical MAX fold, disulfide bond patterns and decorating
37 secondary structures in N- and C-terminal extensions. About one-third of the MAX
38 family members remain single, showing no obvious structural relationship with other
39 MAX effectors. Analysis of the surface properties of the AF MAX models also
40 highlights the very high variability remaining within the MAX family when examined at
41 the structural level, probably reflecting the wide diversity of their virulence functions
42 and host targets.

43

44 **Author summary**

45 MAX effectors are a family of virulence proteins from the plant pathogenic
46 fungus *Pyricularia* (*syn. Magnaporthe*) *oryzae* that share a similar 3D structure
47 despite very low amino-acid sequence identity. Characterizing the function and
48 evolution of these proteins requires a detailed understanding of their structural
49 diversity. We used a combination of experimental structure determination and
50 structural modeling to characterize in detail the MAX effector repertoire of *P. oryzae*.
51 A prediction pipeline based on similarity searches and structural modeling using the
52 AlphaFold2 (AF) software were used to predict MAX effectors in a collection of 120
53 *P. oryzae* genomes. We then compared AF models with experimentally validated
54 NMR structures. The resulting models and experimental structures revealed that the
55 preserved MAX core coexists with extensive structural variability in terms of
56 structured N- or C-terminal extensions. For each of the AF models, we also analyzed
57 the surfaces of the canonical fold that may be involved in protein-protein interactions.
58 This work constitutes a major step in mapping the functional network of MAX
59 effectors through their structure by identifying possible recognition sites that may help
60 focusing studies of their putative targets in infected plant hosts.

61

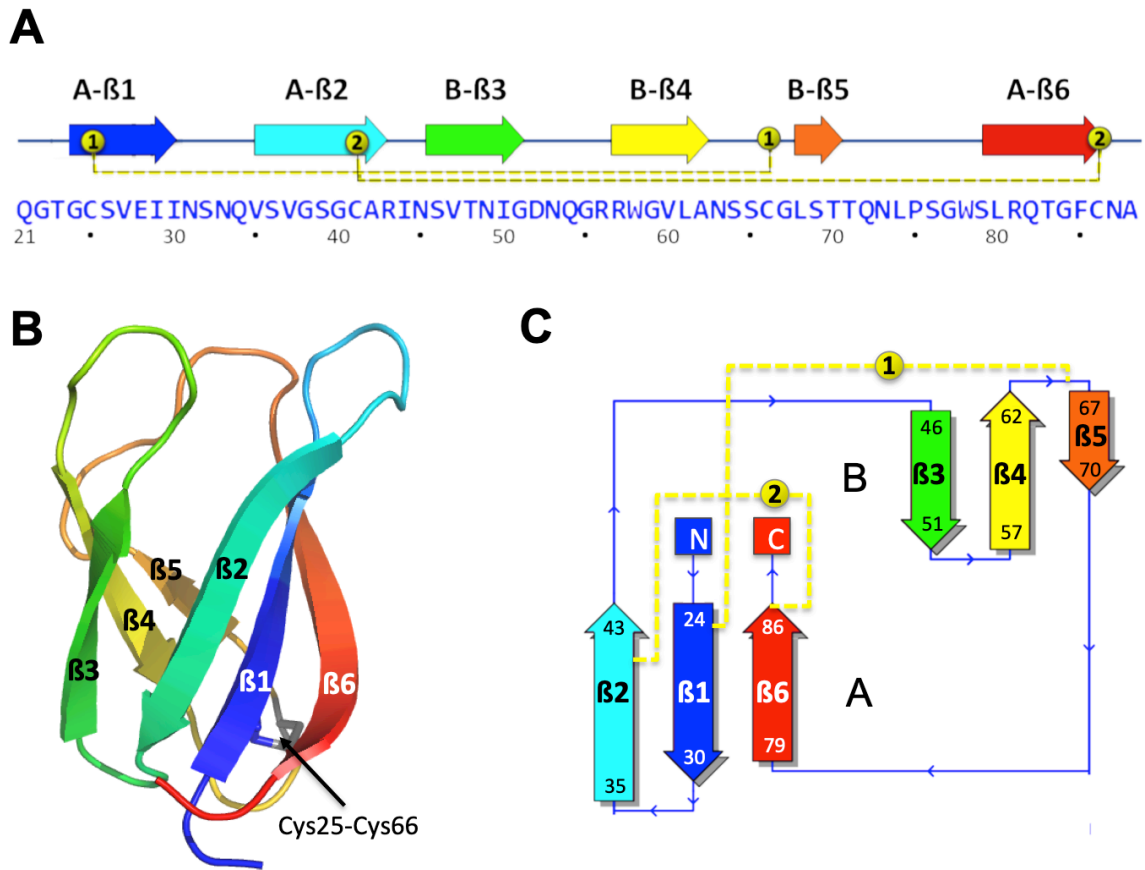
62 Introduction

63 Fungal plant pathogens secrete small proteins, called effectors, which promote
64 disease by targeting cellular processes in the host plant. These fungal effectors are
65 usually identified based on their secretion signal and other features such as cysteine
66 enrichment [1,2]. There are hundreds of predicted effectors in the genomes of plant
67 pathogenic fungi and very few of them show sequence similarities and/or homology
68 to known proteins or protein domains. Some effectors are of particular interest since
69 they constitute avirulence (AVR) factors that can be detected by plant immune
70 systems and render crops resistant to severe diseases. Because fungal effectors
71 usually show no amino-acid sequence homology to known proteins or protein
72 domains, their biological function cannot be inferred from systematic *in silico* analysis
73 (such as domain searches) but has so far been elucidated on a case-by-case basis.
74 As a huge and growing number of putative effectors is being discovered, deciphering
75 the functions and adaptive evolution of fungal effectors thus requires robust
76 predictive tools for analyzing protein sequences and identifying candidates on which
77 prioritize functional and structural studies.

78 Recently, a combination of primary sequence pattern searches and structural
79 modeling resulted in a major breakthrough in the study of effector biology by
80 revealing that fungal effector repertoires are actually dominated by a limited number
81 of families sharing common structures despite extensive sequence variability [3–5].

82 One such family is the superfamily of MAX (*Magnaporthe* AVRs and ToxB-like)
83 effectors we identified in *Pyricularia oryzae* (synonym: *Magnaporthe oryzae*), the
84 fungus causing blast disease in rice, wheat, and other cereals or grasses. This
85 pathogenic fungus is both a major threat to global food security and a prime

86 experimental model in plant pathology because of its ability to rapidly evolve to
87 escape recognition of the plant immune system. By solving the solution structure of
88 two *P. oryzae* effectors, AVR1-CO39 and AVR-Pia, we discovered strong structural
89 similarities between these sequence-unrelated effectors as well as with the ToxB
90 effector from the wheat infecting fungus *Pyrenophora tritici-repentis* [6]. This latter
91 showing sequence homology with a putative effector from *M. oryzae*, we solved the
92 crystal structure of this MoToxB protein (supplementary materials and methods) and
93 confirmed its structural similarity with ToxB as well as with the other structurally
94 determined *P. oryzae* MAX effectors that together with MoToxB share less than 13%
95 sequence identity (S1 Fig). Like other MAX effectors, MoToxB is structured as a 6-
96 stranded β -sandwich (β 1 to β 6) of two triple-stranded β -sheets with a β 6 β 1 β 2-
97 β 3 β 4 β 5 topology. The highly conserved disulfide bond forms a bridge between β 1
98 and the loop connecting β 4 and β 5 while a second disulfide bond connects β 2 and
99 β 6 (Fig 1).



100

101 **Fig 1. Structure of the *M. oryzae* ToxB (MoToxB) MAX effector**

102 Primary and secondary structure of MoToxB showing the triple-stranded beta-sandwich
 103 forming the conserved MAX core with the two beta-sheets labeled by A and B, strands
 104 indicated by arrows and two disulfide bonds in yellow dotted lines. Disulfide bond “1”
 105 almost strictly conserved in MAX effectors. (B) Cartoon representation of MoToxB crystal
 106 structure (PDB 6R5J) shown in rainbow color and the conserved disulfide bond “1” shown in
 107 sticks. (C) MoToxB topology diagram drawn by PDBsum and colored using the same color
 108 scheme as in A and B.

109

110 MAX effectors are specific to plant pathogenic ascomycetes fungi and they
 111 have undergone a major expansion in *P. oryzae*, suggesting an important role in the
 112 infection process. Our recent analysis of 120 isolates of *P. oryzae* identified 58 to 78
 113 MAX effector genes per genome, corresponding to 5 to 10% of the full repertoire of
 114 predicted effectors. In addition to this genetic expansion, the importance of MAX

115 effectors in *P. oryzae* virulence is supported by our finding that many MAX effectors
116 are massively expressed during the early stages of plant infection in a host-
117 dependent manner [5–7]. They are also specifically targeted by the plant immune
118 system: nearly half of the cloned avirulence genes of *P. oryzae*, which encode
119 avirulence (AVR) factors recognized by host resistance proteins in blast disease
120 resistant cultivars, correspond to MAX effectors [6,8–11]. Analysis of the recognition
121 of the MAX effectors AVR-Pia, AVR1-CO39, and AVR-Pik by rice immune receptors
122 indicates that they may target a specific class of proteins called small HMAs (sHMAs)
123 [12], which show similarity to copper chaperones containing a heavy metal-
124 associated domain (HMA). Experimental evidence supports this hypothesis in AVR-
125 Pik, but the sHMA proteins' biological function and role in the infection process are
126 unknown. Another MAX effector, AvrPiz-t, targets four different host proteins involved
127 in different cellular processes [13,14].

128 In our previous study, we have explored the genetic diversity of the MAX
129 effector family in different *P. oryzae* host-specific lineages [7] in order to get insights
130 into the adaptive evolution and the selective forces that shape the molecular
131 variability of structurally analogous effectors. Focusing on the variations observed
132 within the predicted conserved MAX core, we identified a total of ~7800 orthologous
133 and paralogous sequences of putative MAX effectors clustered in 94 orthogroups
134 (OG). Pan-genome analyses showed that the MAX effector repertoire is highly plastic
135 compared to other secreted proteins, both in terms of the presence/absence of
136 orthogroups and the sequence variability within OG clusters. Interestingly, mapping
137 of polymorphic residues for the three effectors whose binding interfaces have been
138 experimentally characterized (AVR1-CO39, AVR-Pia and AVR-Pik) [7] suggests that

139 amino acid changes often co-localized with residues interacting with immune
140 receptors and, presumably, also with their host target proteins.

141 In order to further exploit the structure-based repertoire of *P. oryzae* MAX
142 effectors and get a complete view of their molecular diversity, a systematic and
143 robust analysis of their three-dimensional structure, especially outside the MAX core
144 domain, is still needed. Such analysis could allow a more comprehensive
145 classification of effector proteins within the MAX family and provide information on
146 how MAX effectors evolve and adapt to specific hosts. Indeed, many MAX effectors
147 possess N- and C-terminal extensions that could establish specific protein-protein
148 interactions playing a key role in the function of MAX effectors and their interference
149 with different host molecular processes. Examining in more details these extensions,
150 as well as other non-conserved structural features, may thus provide insights into the
151 mechanism by which MAX effectors acquire new virulence capabilities.

152 In the present study, we combined experimental and computational
153 approaches to finely characterize the structural diversity of MAX effectors. In order to
154 evaluate the reliability of the homology modeling approach we previously used for
155 predicting MAX effectors, we undertook structural studies of several MAX candidates
156 and succeeded in solving four new structures by Nuclear Magnetic Resonance
157 (NMR). Comparison of the new experimental MAX structures with their
158 corresponding 3D models generated by template-based or *ab initio* modeling
159 programs revealed the high accuracy with which AlphaFold2 (AF) can predict the
160 structure of MAX effectors, including for non-conserved side-chains in terminal
161 extensions that were not previously observed. We therefore revisited with the use of
162 AF the structural landscape of *P. oryzae* MAX effectors and validated the presence of
163 a MAX core in 77 of the 94 MAX OG clusters defined in Le Naour--Vernet et al. 2023

164 [7]. Structural alignment of the AF models allow us to describe the structural
165 consensus and variability within the MAX family, from the canonical fold, but also
166 including disulfide bond pattern variations, decorating secondary structures within the
167 N- and C-terminal extensions that may be involved in protein-protein interactions as
168 well as surface properties, including stickiness and electrostatics of the core domain
169 of MAX effectors.

170 This work represents the most extensive structural analysis of a fungal effector
171 family of a plant pathogen to date. It also provides valuable knowledge for analyses
172 aimed at elucidating the function of MAX effectors, notably through the prediction of
173 interaction sites within the MAX fold that could contribute to targeting host proteins
174 during infection.

175

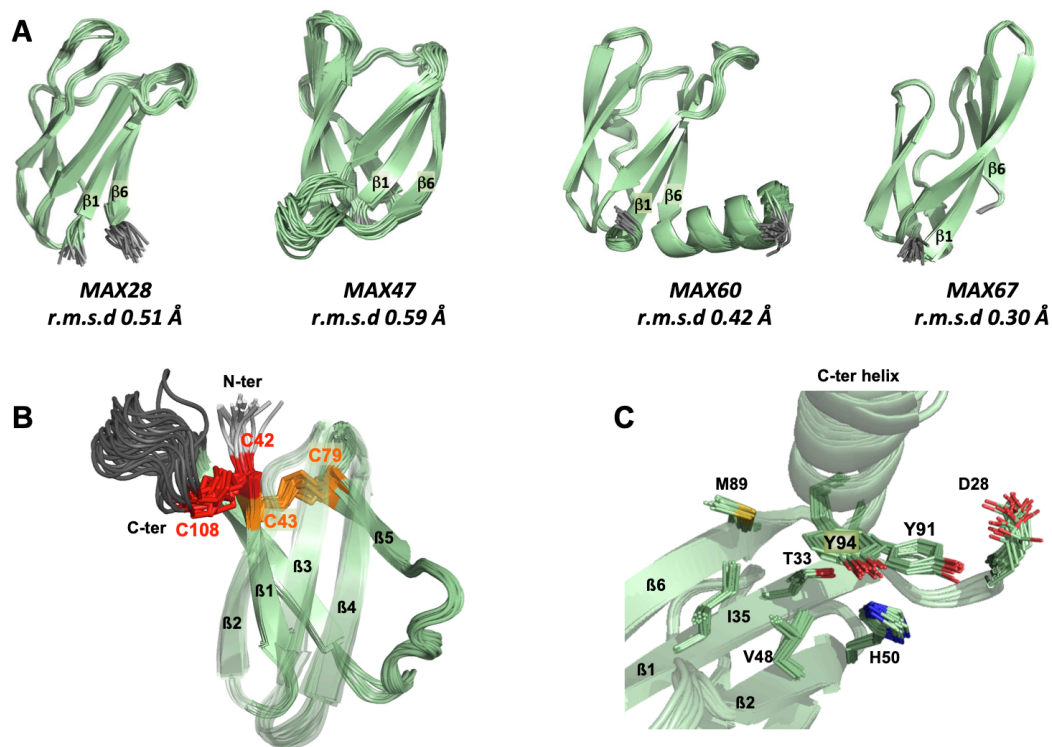
176 Results

177 ***NMR structures validate template-based modeling of MAX effectors***

178 In our previous phylogenetic analysis of the MAX effector repertoire in *P. oryzae*,
179 we used a hybrid multiple Template Modeling (TM) strategy for predicting the 3D
180 structure of the conserved MAX core of representative sequences of 94 orthogroups
181 (OG) and we evaluated the reliability of these 3D models (referred as TM-pred
182 models) by calculating the TM-pred score [7]. The TM-pred score is an estimate of the
183 TM-score given by TM-align superimposition [15] that would be observed when
184 structurally aligning the TM-pred model with the corresponding experimentally
185 resolved structure. At the time this analysis was performed with only 8 experimental
186 structures of MAX effectors used as templates for homology modeling in a training
187 data set used to set-up of the TM-pred scoring function [7]. From the online table
188 <https://pat.cbs.cnrs.fr/magmax/model/> (see also Materials and Methods) can be
189 downloaded the TM-pred models and their TM-pred scores calculated for the
190 predicted MAX core of 94 OG proteins (i.e. selected representative sequences of
191 MAX OG clusters, as listed in the S2 Table). Comparison of the TM-pred scores
192 shown in the S1 Fig indicates that ~90% of the OG proteins could be modeled with a
193 MAX structure having a predicted accuracy exceeding a TM-pred score > 0.6,
194 whereas only three TM-pred models of OG proteins (OG22, OG77 and OG85) had a
195 TM-pred score below 0.5 and were rejected as MAX effectors.

196 In order to assess the validity of these predictions, we aimed to resolve new
197 experimental structures not included in the set of templates used in training the TM-
198 pred score. We attempted to express genes corresponding to mature proteins from
199 10 OG clusters was attempted (S3 Table) for MAX effector candidates showing high
200 expression level during the biotrophic stage of infection [7]. Using NMR spectroscopy

201 we successfully determined the structure of four OG cluster representatives (OG28,
202 OG47, OG60 and OG67) and we confirmed that all four proteins are MAX effectors
203 (referred to as “MAX” instead of “OG clusters” from hereon). The 20 best-refined
204 conformers obtained for each of these effectors were superimposed (Fig 2A) and the
205 low root mean square deviations (r.m.s.d) support the high quality of the NMR
206 structures. The complete structural statistics are given in S4 Table.
207



208

209 **Fig 2. NMR structures of four MAX effectors.** (A) NMR structures of MAX28, MAX47,
210 MAX60 and MAX67 showing the superimposition and the r.m.s.d. of their 20 best
211 conformers. The N- and C-terminal unstructured extensions before β1 and after β6,
212 respectively, are not shown. (B) View of the two disulfides bonds, C42-C108 (red) and C43-
213 C79 (orange) for NMR structure of MAX47. The loop between the end of β6 and the C-
214 terminus is colored in dark grey. The β2, β3 and β4 strands are transparent. (C) Local
215 environment of the two residues Y91 and Y94 in the C-terminal helix of MAX60.

216

217 Among the four MAX effectors, three proteins (MAX28, MAX47 and MAX67)
218 displayed the characteristic MAX β -sandwich fold consisting of two triple-stranded β -
219 sheets stapled against each other through a conserved disulfide bridge linking β 1
220 and the β 4- β 5 loop (Fig. 1). The two cysteine residues forming this salt bridge are the
221 only residues that are highly conserved in MAX effectors. In MAX67, the β 1 and β 2
222 strands are longer than (10 a.a.) than their counterparts previously observed in other
223 MAX structures. A slight divergence from the canonical MAX fold was observed for
224 MAX60: the β 5 strand is replaced by a helical turn that prevents the formation of a
225 regular β -sheet with β 4. In addition to the central MAX core, MAX28, MAX47 and
226 MAX60 presented remarkable N- and C-terminal extensions. For MAX47, the 23
227 residue-long N-terminal sequence extending before the β 1 strand was enriched in
228 serine residues and was not resolved in the NMR structure. The β 1 strand starts with
229 two consecutive cysteine residues. The first cysteine makes a disulfide bond with the
230 last C-terminal cysteine residue (C42-C108). The second cysteine in β 1 forms a
231 disulfide bond with the cysteine in the β 4- β 5 loop (C43-C79) as expected in
232 canonical MAX effectors. Both disulfide bonds are well defined in the NMR structure
233 (Fig 2B). MAX60 has a C-terminal extension, which forms a well-defined α -helix. This
234 C-terminal helix is attached to the structural core by hydrophobic contacts with the
235 rings of two tyrosine residues (Y91 and Y94). In the NMR experiments, close
236 contacts deduced from Nuclear Overhauser Effects (NOEs) data were found
237 between residues D28 to T33 and H50 for tyrosine Y91, and residues T33, I35, V48
238 and M89 for tyrosine Y94 (Fig 2C). In case of MAX28, cleavage of the His-tag after
239 affinity chromatography resulted in the precipitation of the protein that could not be
240 purified with sufficient quality for structural studies. Nonetheless, the N-terminal His-
241 tagged version was amenable to NMR analysis (Material and Methods). The 42

242 residue long C-terminal extension of MAX28 contains lysine-repeated motifs (KxxxK)
243 and was predicted to be unstructured. The corresponding resonances were not
244 assigned in the NMR spectra.

245

246 The four new NMR structures of MAX effectors were superimposed using TM-
247 align with the corresponding TM-pred models that we previously generated by
248 template homology modeling (Fig 3A). The quality of the models can be evaluated by
249 the root-mean-square deviation (r.m.s.d) calculated between the observed and
250 predicted structures and the TM-scores given by TM-align (a value of 1 meaning a
251 perfect match). Comparison of the superimposed backbones shows that the overall
252 MAX fold as well as the relative orientation of the two β -sheets forming the central β -
253 sandwich were all well predicted, especially in the case of MAX28 for which the TM-
254 pred model of the MAX domain matches very well the experimental structure
255 (r.m.s.d.=2.11 Å), even for the loops joining the β -strands. MAX28 was also the
256 effector with the highest estimated TM-pred score (0.75), in remarkably good
257 agreement with the true TM-score (0.74) of the TM-pred model aligned to the NMR
258 structure. Structural predictions of the MAX core were also very good for MAX67,
259 except for the long strands β 1 and β 2 observed in the NMR structure that could not
260 be accurately modeled, explaining the rather low TM-pred value proposed for TM-
261 pred_MAX67. Some β -strands were also poorly defined in case of MAX47 and
262 MAX60 whose models, compared to the NMR structures, exhibit also strong
263 divergence for the connecting loop regions. For MAX47, the low reliability of the TM-
264 pred model was anticipated by the TM-pred score (0.63).

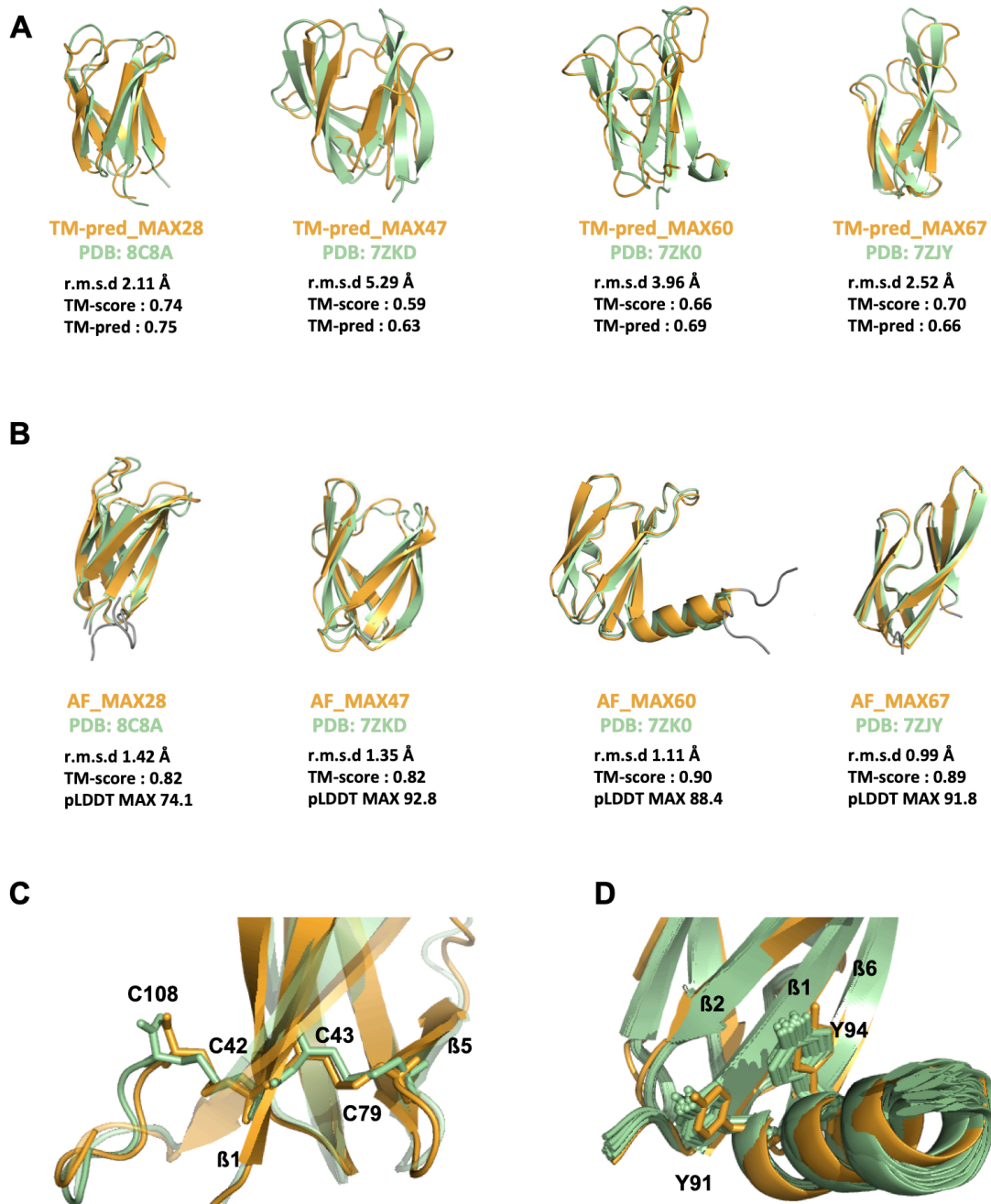
265

266

267 ***AlphaFold2 reliably predicts MAX effectors core and extensions.***

268 The recent release of Artificial Intelligence (AI)-based methods have
269 demonstrated the high accuracy with which deep-learning software such as
270 AlphaFold2 (AF2) can predict the 3D structure of most *structured* proteins [16]. We
271 therefore decided to test the accuracy of AF2 to predict MAX effector structures by
272 submitting the amino acid sequences corresponding to MAX28, MAX47, MAX60 and
273 MAX67 for which the coordinates of the NMR structures we determined had not yet
274 been released in the PDB. We used three different implementations of AF2 to
275 generate the multiple sequence alignment (MSA) from which protein 3D models are
276 predicted. The MMseqs2 and Jackhmmer implementations use MSAs generated
277 automatically online or locally and that can include PDB templates, whereas the
278 *Custom* MSA implementation uses MSAs provided by the user and was
279 parameterized to not use PDB templates (see Materials and Methods). For each
280 sequence query, the three MSAs were independently submitted to AF2 and the
281 predictive quality of the top-ranked models was assessed thanks to the predicted
282 local distance difference test (pLDDT) [16,17]. The pLDDT score scaling from 0 to
283 100 is a residue-level accuracy score computed by AF2 that provides an estimate of
284 the confidence of each residue's predicted position in the protein structure. We
285 considered the average pLDDT score for the overall protein, or only for residues
286 within the predicted MAX core domain, herein called the MAX pLDDT score. The
287 MAX pLDDT score allows better filtering of the AF-generated models, since it
288 provides a quantitative measure of prediction quality focusing on the MAX core
289 domain. For each MAX effector, the AF model having the highest MAX pLDDT score
290 was selected and referred as its AF_MAX model (Fig 3).

291 The MAX core domain was very well predicted in AF_MAX47, AF_MAX60 and
292 AF_MAX67 according to their high MAX pLDDT scores, close to or exceeding 90 (Fig
293 3B and S5 Table). All the three selected models were obtained from the Jackhmmer
294 AF2 implementation. Lower confidence score (74.1) was retrieved for the best AF2
295 model of MAX28, generated using the *Custom* MSA implementation. Nevertheless,
296 AF_MAX28 was very close to MAX28 experimental structure according to the
297 average r.m.s.d. value (1.42 Å) calculated when superimposing the MAX core
298 backbone atoms of the NMR conformers. Indeed, for all four MAX effectors, the MAX
299 domain of the selected AF model displayed side-chain rotamers very similar to those
300 observed in the experimental structures within the uncertainty of the NMR approach,
301 i.e. density of NMR-derived constraints (Fig 3B).



302

303

304 **Fig 3. Comparison of newly determined NMR structures of MAX effectors with**
 305 **their TM-pred or AF predicted models.** Superimposition of the four MAX effectors
 306 determined in this study by NMR shown by the best model (in green) and of their
 307 corresponding 3D models (in orange) predicted by hybrid multiple template modeling (TM-
 308 pred models shown in A) or AlphaFold2 (AF models shown in B). Metrics used for the
 309 quantitative assessment of the similarities between the predicted 3D models and their
 310 respective experimental structures are indicated: the root mean square deviation (r.m.s.d; the
 311 lowest, the best), the template modeling score (TM-score from TM-align, a value of 1

312 corresponding to a perfect match), *TM*-pred score (a predictive estimate of the *TM*-score).
313 The N- and C-terminal boundaries were set according to the *TM*-pred models and did not
314 include extensions determined in the NMR structures. (B) The r.m.s.d. between backbone
315 heavy atoms of the superimposed NMR structure and AF models is given for the MAX
316 domain only (Table S5), as well as the predicted local distance difference test (pLDDT) that
317 was used to estimate the reliability of the AF predictions in the MAX core (MAX pLDDT
318 score, Table S5). (C) View of the two disulfides bonds of MAX47, C42-C108 and C43-C79,
319 as observed in the best NMR conformer and in the predicted AF_MAX47 model. (D) Local
320 environment of the two tyrosyl side-chains of Y91 and Y94 in the C-terminal helix of MAX60
321 in the 20 NMR conformers and in AF_MAX60.

322
323 AlphaFold2 modeling also succeeded in predicting details within the core
324 domains. The cysteine residue side-chains forming the conserved disulfide bond “1”
325 are well defined in all four MAX effector models, as well as those forming an
326 additional SS bond bridging the N- and C-terminal extensions in the experimental
327 structure of MAX47 (Fig 3C). Another example of consistency between experimental
328 structures and AF models was the remarkably well-defined position and orientation of
329 the C-terminal helix of MAX60, in particular for two tyrosine residues whose aromatic
330 side chains stack over the β 1- β 2- β 6 β -sheet of the MAX core (Fig 3D). For MAX28,
331 both AF model and NMR structure were consistent in predicting unstructured N- and
332 C-terminal extensions. Moderate deviations from the experimental structure were
333 observed for residues in the C-terminus of MAX67 (S2 Fig).

334

335 ***Family portrait of AlphaFold2 MAX models***

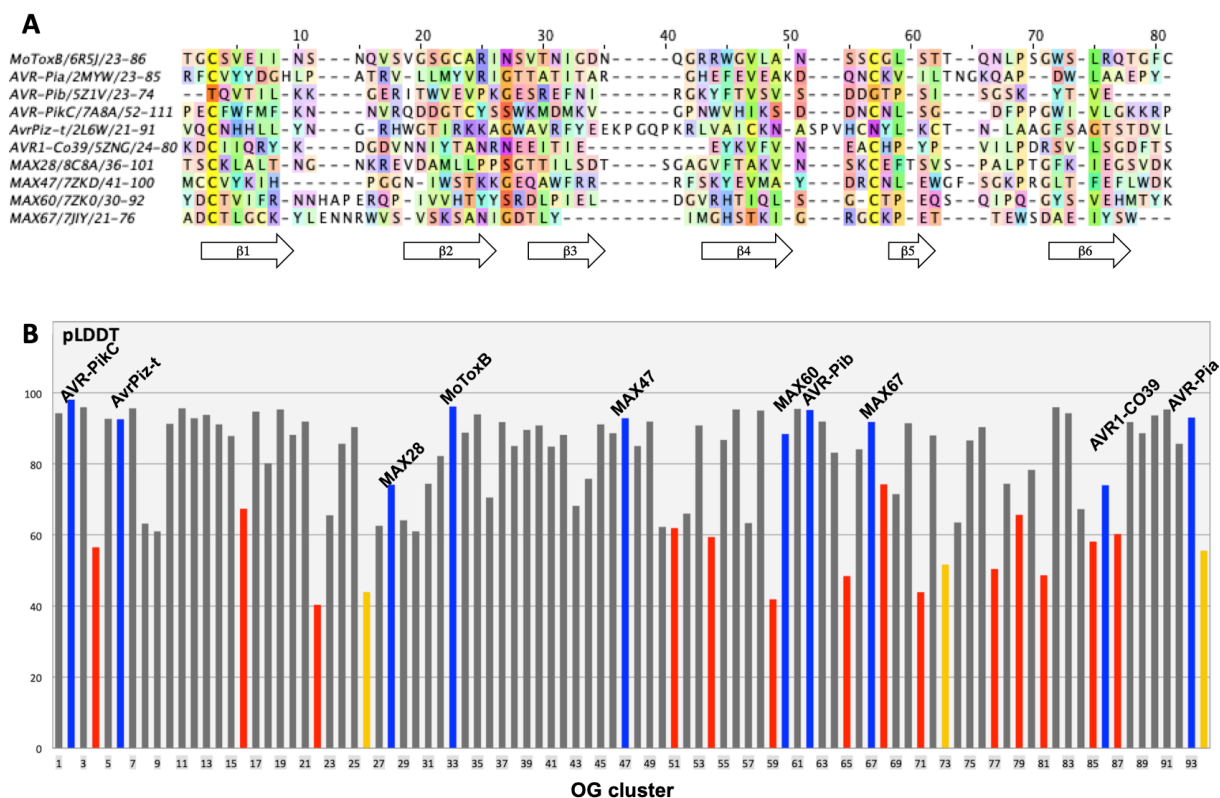
336 Given the high predictive quality of the AF-generated models of MAX effectors,
337 we applied the same AF modeling strategy to all other *P. oryzae* OG representative
338 members. The models were visualized to check the presence of the characteristic
339 MAX core by inspecting the β -strand topology and formation of the conserved SS “1”
340 disulfide bond (Pymol. v.1.6; Delano 2002). OG proteins showing significant

341 topological deviations from this canonical MAX fold were discarded. The strict
342 presence of the short β 5 strand was not used as a filtering criterion. Among the 80
343 AF models that matched the canonical MAX structure (Fig 4), 57 had MAX pLDDT
344 scores greater than 80 and 20 had MAX pLDDT scores ranging from 60 to 80. Only
345 three OG proteins, OG26, OG73 and OG94, exhibiting a central core compatible with
346 a MAX fold had a MAX pLDDT score below 60 and were not kept in our final
347 selection of 77 validated MAX structures.

348 Among the 14 OG proteins that are not predicted to fold with the MAX
349 topology, three (OG22, OG77 and OG85) were previously rejected based on their
350 low TM-pred score and five (OG04, OG59, OG65, OG68 and OG81) had a TM-pred
351 score under 0.6 (S1 Fig). Other OG proteins such as OG51 and OG54 that exhibited
352 a TM-pred score above 0.6 compatible with a MAX structure displayed significant
353 distortions from the canonical MAX fold when modeled by AlphaFold2.

354 For OG51, two models computed with MMseqs2 and the AF Jackhmmer
355 implementation gave very similar models (backbone r.m.s.d. of 1.77Å) with pLDDT
356 overall scores of 52.6 and 61.9, respectively. However, the C-terminal β -strand of
357 OG51 had a parallel orientation relative to the first β 1 strand that was not compatible
358 with the MAX topology. The best OG54 model had a pLDDT score of 59.4 but
359 deviated from the MAX topology by the absence of the C-terminal β 6 strand, which
360 was not accurately modeled.

361



362

363 **Fig 4. pLDDT scores of AF models for known and predicted MAX effectors.**

364 (A) Structural alignments of experimentally determined MAX effector structures using
 365 MoToxB structure for reference. Residues are colored according to the Taylor scheme
 366 [18](Taylor, 1997) and conservation (above 15% threshold) is used as a shading factor.

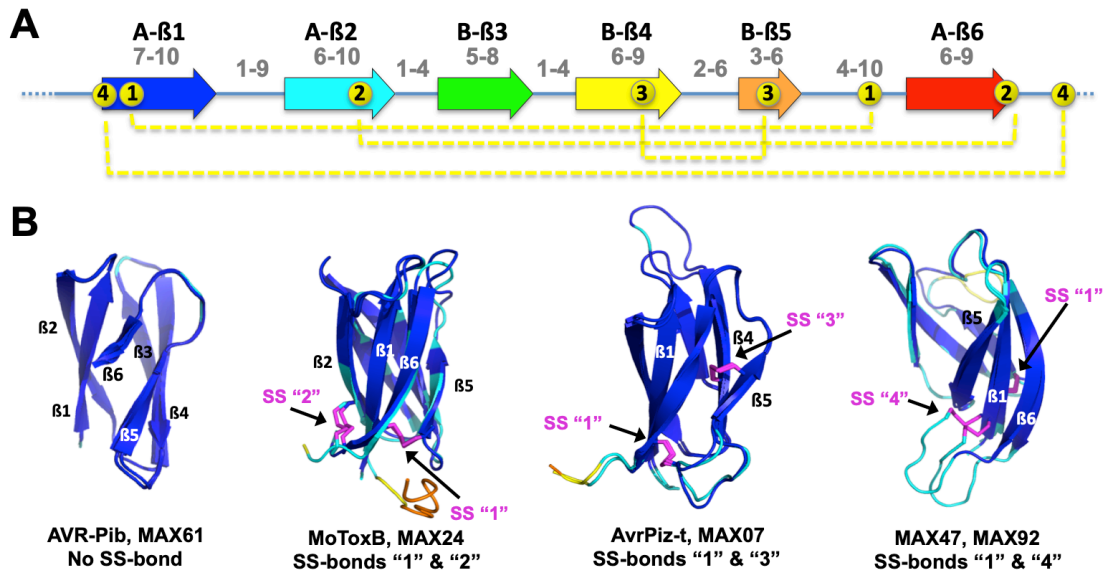
367 (B) pLDDT scores of the best AF models selected for the 94 OG clusters of predicted MAX
 368 effectors with experimentally determined structures in blue, and OG clusters that displayed
 369 canonical MAX folds in grey. For these OG clusters we report the best MAX pLDDT score.
 370 OG clusters represented in red are the ones for which none of the models matched the
 371 canonical MAX fold, and in such cases we report the best overall pLDDT score of the model.
 372 MAX pLDDT scores of models that have a canonical MAX fold but a score below 60 are
 373 shown in orange. Full data is available in S5 Table.

374

375 The 14 OG clusters that gave inconclusive AF models were submitted to two
 376 other protein structure prediction web-servers, RaptorX [19] and RosettaFold [20].
 377 None of the computed models displayed the canonical MAX fold, confirming that
 378 these OG cluster sequences were difficult to model and quite probably do not exhibit
 379 the expected MAX topology.

380 ***Variations around the canonical MAX fold***

381 A statistical overview of the general structural features characterizing the 77
382 AF models of validated MAX effectors is given in Tables S7a and S7b. A unique
383 member of the MAX family is MAX52, whose AF model consists of two MAX core
384 modules in tandem. The MAX52 model was cut into two chains (MAX52A and
385 MAX52B), each corresponding to a MAX core domain. In Fig 5A is indicated the
386 average size of the β strands and connecting loops forming the conserved 6
387 stranded β sandwich that defines the canonical MAX fold, well represented by the
388 MoToxB (MAX33) structure. β 1 and β 2 are usually of similar size and associate
389 together with β 6 to form the longest anti-parallel β sheet, while β 3 and β 4 strands are
390 usually shorter. Substantial variations around this common fold can be observed,
391 notably in the C-terminal part of the MAX core where the short β 5 strand can be
392 totally absent (MAX78 and MAX83) or replaced by a helix (MAX20), whereas the β 5
393 strand can range from 2 to 8 residues following a loop that can have up to 25
394 residues (MAX29) or present a short helix (MAX15, MAX60). The number of disulfide
395 bonds stabilizing the protein can also greatly varied (Table S7a), from none in
396 MAX61 and MAX62 (AVR-Pib) to three in MAX46 or four in MAX52. Besides of the
397 conserved disulfide bond (SS "1"), which is a hallmark of the MAX domain, three
398 types of additional disulfide bonds (SS "2", "3" and "4") are found in the observed or
399 AF predicted MAX structures (Figs 5A and B). SS "4", joining the N-terminus of β 1 to
400 a C-terminal cysteine, is well defined in both MAX47 and MAX92, although it was not
401 present in any of the previously determined MAX 3D structures that could serve as
402 template. This disulfide bond was experimentally validated by our NMR structure of
403 MAX47.



404

405 **Fig 5. MAX domain structural features.** (A) Average size range (indicated in grey) of β
 406 strands (arrows) and connecting loops forming the central β sandwich of the canonical MAX
 407 core, and of the N-ter and C-ter extensions. Average ranges are calculated in Table S7b.
 408 The 4 different types of disulfide bonds observed in MAX structures and models are indicated
 409 by dotted yellow lines. (B) Four different sets of structural models illustrating the variability of
 410 disulfide bond patterns. The AF models are colored according to their pLDDT score, by blue
 411 for high accuracy (>90), cyan for backbone at good accuracy (> 70), yellow for low
 412 confidence (> 50 and < 70) and orange for disordered (< 50). The disulfide bonds are shown
 413 in magenta, except for the AVR-Pib structure, which does not have a disulfide bond.

414

415 **N- and C-terminal extensions**

416 Over two-third of the 77 AF_MAX models possess peptide segments with 15
 417 or more residues extending at one or both ends of the central MAX domain (Table
 418 S7a and S7b). Diverse length of these extensions, especially in C-terminal, can be
 419 observed among OG sequences belonging to the same OG cluster (e.g. OG01,
 420 OG02 or OG15 clusters in Table S1a). C-terminal extensions are also more
 421 numerous and usually longer than N-terminal extensions. They are often modeled by
 422 AF2 with well-defined secondary structures, such as additional β strands extending
 423 the $\beta 2\beta 1\beta 6$ sheet by one or two strands (e.g. MAX08, MAX12, MAX25), or a terminal

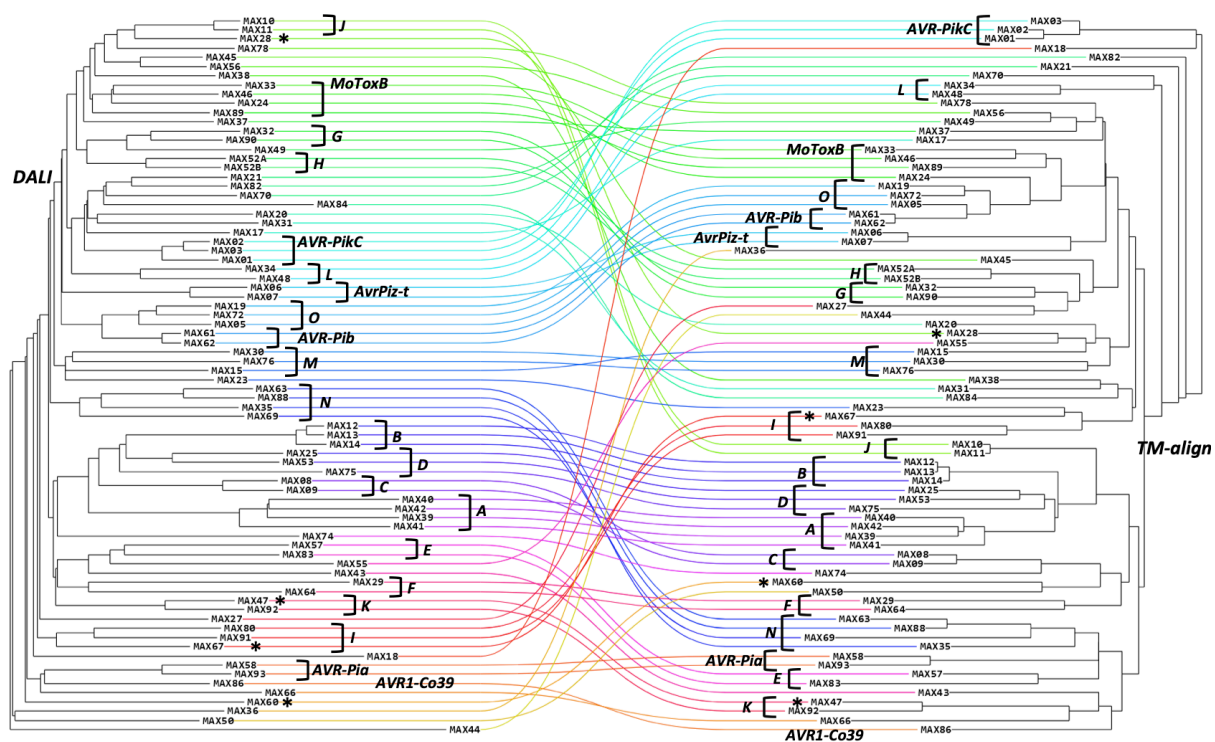
424 helix as observed in the model and solution structure of MAX60. There are also many
425 examples where terminal extensions appear as unstructured regions that could not
426 be modeled with high confidence by AlphaFold2. Long intrinsic disordered regions
427 (IDRs) of more than 30 a.a. [21–23] may have diverse function in bacterial [24,25]
428 and fungal effectors [26,27] and we had therefore searched for IDR signatures in
429 MAX effector sequences using ESpritz prediction software [28]. Long IDRs were
430 predicted for only a few MAX effectors and their presence was cross-validated for six
431 AF_MAX models: in MAX15 (118 a.a.), MAX27 (36 a.a.) and MAX43 (43 a.a.) as N-
432 ter extensions, and in MAX28 (42 a.a.), MAX53 (49 a.a.) and MAX78 (43 a.a.) as C-
433 ter extensions. It thus appears that long IDRs is not a frequent feature among *P.*
434 *oryzae* MAX effectors, present in less than 8% of all modeled structures. The NMR
435 solution structure of MAX28 validated the unstructured nature of its C-terminal
436 extension.

437

438 ***Structural classification of MAX effectors***

439 Structural similarities between proteins can help to elucidate the function of an
440 uncharacterized protein and infer its molecular evolution. Here we performed
441 hierarchical clustering of the selected 77 MAX effector models with two protein
442 structure alignment software, Dali [29] and TM-align [15,30] which use different
443 criteria for similarity scoring of superimposed structures. The Dali Z-score relies on
444 secondary structure pairing and is a good estimate of topological conservation while
445 the TM-score is computed for the whole alignment and weights paired residues with
446 low r.m.s.d. more strongly than those that are more distant. When analyzed
447 independently, the structural alignment trees retrieved from these two clustering
448 approaches did not reveal clear sub-families of MAX structures, as shown by the lack

449 of long internal branches in Fig 6. To facilitate the comparison of the trees, we
 450 differently colored the lines connecting each MAX model in both trees (see Materials
 451 and Methods).
 452
 453






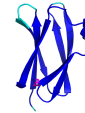

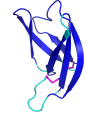


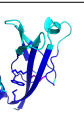





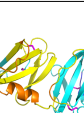





454
 455 **Fig 6. Comparison of the structural similarity trees of MAX effectors based on**
 456 **the Dali Z-score (left) and TM-alignTM-score (right) of their superimposed AF**
 457 **models.** Unstructured N- and C-terminal regions were removed from the AF_MAX models
 458 prior to the analysis. A line of a specific color connects each AF_MAX model in the Dali and
 459 TM-align trees. The MAX effectors with an experimental 3D structure are indicated by their
 460 name, or a star for the four novel MAX structures. The structural groups to which the MAX
 461 effectors were assigned are indicated by brackets and illustrated in Table 1 and S3 Fig.
 462

463 In this representation, any bundle of lines of similar colors highlights a possible
 464 structural similarity between the models that was common to both clustering methods
 465 and that could define a group of MAX models. Each group of at least two models
 466 was visually inspected for additional secondary structures that could add to the MAX

467 core, the disulfide bond pattern as well as for specific structural features that fall
468 outside the statistical average values reported in Fig 5A. Using this dual clustering
469 method, we defined 15 groups of MAX models sharing common structural features,
470 in addition to the 5 groups of well-established MAX effectors (AVR-Pia, AVR-Pib,
471 AVR-PikC, AvrPiz-t and MoToxB). Groups A to G gather MAX models exhibiting
472 major structured elements adding to the canonical MAX core: groups A and B contain
473 models with 2 extra strands, groups C and D contain models with 1 extra strand, and
474 groups E to G contain models with C-terminal helical extensions after $\beta 6$. Group H
475 consists of the MAX52 tandem domains connected by a structured linker. In contrast,
476 groups I to O correspond to plain MAX structures, without ostentatious decoration but
477 presenting variations of the MAX fold specific to each group. The characteristics of
478 this total of 20 MAX structural groups are summarized in Table 1 and illustrated with
479 more details in S3 Fig. Only 6 groups exhibits a disulfide bond pattern with a specific
480 SS bond adding to the conserved SS"1", and only the AVR-Pib group has no SS
481 bond. The MAX models listed in Table 1 represent about two-third of the 77 MAX
482 effectors that we validated in the present analysis. Several of them had been
483 identified in a previous computational structural genomics study of *M. oryzae* strain
484 70-15 (see below) and are also listed in Table 1.

485

486 **Table 1. Structural groups identified in *P. oryzae* MAX effector family**

Group	representative structure	MAX Id	SS(*)	Structural Specificities and Extensions	Group	representative structure	MAX Id	SS(*)	Structural Specificities and Extensions
A		MAX39, MAX40, MAX41, MAX42, MGG_16939T0, MGG_18062T0	1	additional β 7 β 8 strands flanking one side of the β 2 β 1 β 6 sheet and C-terminal extensions after β 8 that are in helical conformations	I		MAX67, MAX80, MAX91, MGG_16175T0	1	long β 1 strand paired with long β 2 or β 6 strands
B		MAX12, MAX13, MAX14, MGG_16619T0	1	additional β 7 β 8 strands flanking one side of the β 2 β 1 β 6 sheet	J		MAX10, MAX11	1	presence of a short helix in the connecting loop between β 5 and β 6
C		MAX08, MAX09	1	presence of the β 7 additional strand running antiparallel to the β 6	K		MAX47, MAX92	1, 4	disulfide bond "4" joining the N-terminus of β 1 and the C-terminal extension
D		MAX25, MAX53, MAX75, MGG_02635T0, MGG_15207T0, MGG_11304T0	1	presence of the β 7 additional strand running antiparallel to the β 6	L		MAX34, MAX48, MGG_15625T0, MGG_08992T0	1, 3	malformed β 2 strand and anti-parallel β 4 β 5 strands stabilized by a disulfide bond
E		MAX57, MAX83	1	long β 1 and β 6 strands, C-terminal helical extensions that are stabilized by hydrophobic interactions	M		MAX15, MAX30, MAX76, MGG_10282T0	1	longer β 1 and β 2 strands and their connecting loops
F		MAX29, MAX64, MGG_17255T0	1	C-terminal helical extensions that are stabilized by local residue-specific interactions (disulfide bond or hydrophobic residues)	N		MAX63, MAX88, MAX35, MAX69, MGG_02207T0	1	unusually long loop making the connection between strands β 2 and β 3
G		MAX32, MAX90, MGG_08469T0	1, 3	long loop joining the β 1 and β 2 strands and helical C-terminal extensions that are not strictly conserved in their lengths and orientations	O		MAX05, MAX19, MAX72, MGG_12426T0, MGG_14793T0, MGG_18060T0	1	Structurally similar to AVR-Pib.
H		MAX52	1, 3	two MAX domains	AVR-Pib		MAX61, MAX62		Structurally similar to group O models.
AVR-Pia		MAX58, MAX93	1	β 2 strand interaction with HMA (**)	AvrPiz-t		MAX06, MAX07, MGG_18041T0	1, 3	very similar structures with the main difference for the β 3 β 4 connecting loop
AVR-PikC		MAX01, MAX02, MAX03, MGG_15972T0	1	β 3 strand and N-terminal extension interacting with HMA (**)	MoToxB		MAX24, MAX33, MAX46, MAX89, MGG_17132T0	1, 2	Structurally similar to ToxB with disulfide bond "2"

487 The AF models are colored by their pLDDT scores (see legend of Fig 5). The groups with
 488 major structural variations (addition of secondary structures) are listed in the left-hand
 489 panels, including the MAX domain duplication of MAX52. The remaining groups, from I to O
 490 that do not have additional secondary structures but displayed specific structural variations of
 491 the MAX core domain itself are shown in the right-hand panels. To complete the overview,
 492 the five groups of well-established MAX effectors (AVR-Pia, AVR-Pib, AVR-PikC, AvrPiz-t

493 and MoToxB) are shown at the bottom and highlighted in grey color. The MAX Id column
494 gives the AF model identifiers of the MAX effector list reported in the present study
495 (representative MAX model indicated in bold) and the corresponding MAX effectors reported
496 by Seong & Krasileva, 2021 [3]; Seong and Krasileva, 2023 [4]; Yan and Talbot, 2023 [5] in
497 the *M. oryzae* strain 70-15 are referred to by their MGG identifier (S8 Table).

498 (*) Type of disulfide bond as defined in Fig 5

499 (**) from crystallographic structures of complexes

500

501 **Many MAX effectors are singletons**

502 Singletons of MAX effectors are defined as those with no obvious structural
503 relationship to other MAX effectors. They constitute a third (26/77) of the MAX
504 effectors we modeled. In the majority of cases (17), these MAX effectors consist of a
505 simple MAX core with unstructured N- and/or C-terminal extension(s). Among them is
506 AVR1-CO39 (MAX86), which is specifically absent from the *Oryza*-infecting lineage,
507 and whose structure has been experimentally determined. The remaining 9
508 singletons MAX effectors possess very diverse structured extensions besides the
509 folded MAX core domain as illustrated in S4 Fig. Among these MAX effectors,
510 MAX49 was already reported in *M. oryzae* strain 70-15 corresponding to
511 *MGG_08482T0* [5]. In MAX49, N-terminal and the C-terminal helices form a helix
512 bundle structure, not observed in other MAX effector models. MAX74 has an
513 additional $\beta 7$ strand running anti-parallel to $\beta 6$, as observed for group D models.
514 Three other models have a $\beta 7$ strand, i.e. MAX36, MAX43 and MAX66, the latter
515 having long $\beta 1$ and $\beta 6$ strands. Additional C-terminal helices were modeled with
516 good accuracy in MAX55 and MAX60, but not in MAX44 and MAX84.

517

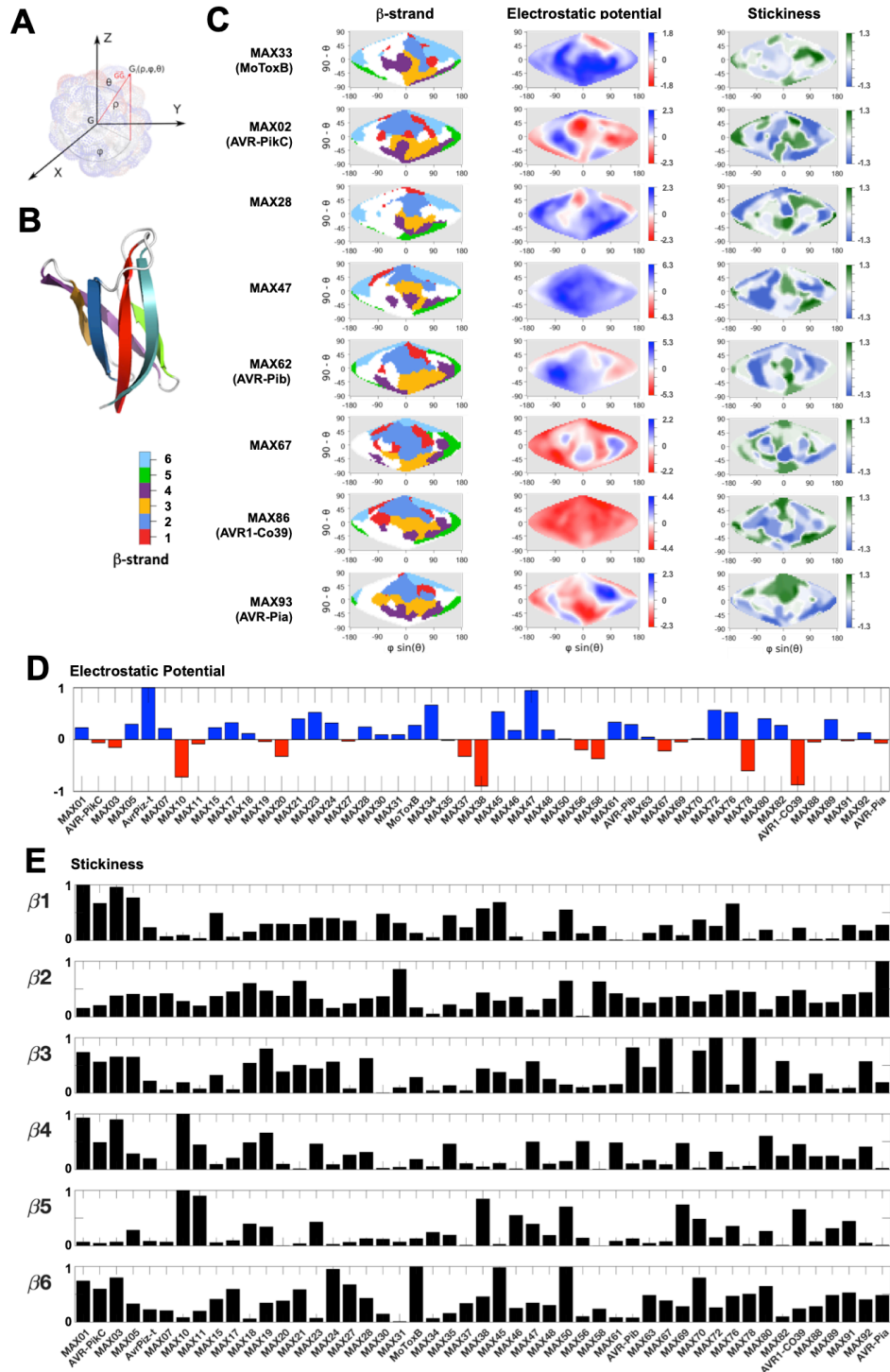
518 **MAX domains exhibit very variegated surface properties**

519 Comparison of the molecular surfaces of homologous proteins can highlight

520 common or specific features related to their function. This can be challenging in case
521 of proteins that differ in size or have structural elements adding to their common fold.
522 Here we have performed a detailed comparative analysis of the surface properties of
523 the standalone MAX domains extracted from 49 AF_MAX models in which no
524 structured regions are predicted to interact with the central core (S7a Table). For this
525 subset of MAX domains, we computed SURFMAP [31] 2D projections of their
526 molecular envelop and compare the distribution of different surface features i.e.
527 exposed secondary structures, electrostatic potential, stickiness (Fig 7) and amino-
528 acid polymorphism within the OG cluster to which belongs each representative MAX
529 model.

530 The β 1-exposed surface is mostly discontinuous around the β 2 surface that is
531 located at the *northern* pole of the projection (Fig 7C). The continuous β 3 surface lies
532 below the β 2 surface and the discontinuous β 4 surface is found at the bottom of the
533 projection. The β 6 surfaces are found to the *west* and *east* of the β 1- β 2 surface
534 areas whereas β 5 surfaces are found on the most *eastern* areas. The electrostatic
535 potential maps (Fig 7D and S2 files) reveal that MAX domain surfaces are more often
536 positively charged than negatively charged or neutral, and that the molecular
537 surfaces can appear entirely positive (e.g. MAX06 (AvrPiz-t), MAX23, MAX34,
538 MAX47) or negative (e.g. MAX10, MAX38, MAX78, MAX86 (AVR1-Co39)), or
539 present intense electrostatic patches (e.g. MAX02 (AVR-PikC), MAX58, MAX62
540 (AVR-Pib), MAX80). It is well known that positively charged regions in proteins are
541 important for interaction with negatively charged macromolecules, such as nucleic
542 acids and lipopolysaccharides [32], whereas negatively charged protein surfaces can
543 be involved in membrane attachment or DNA mimicking functions [33–35]. In
544 MAX47, we noticed that its unstructured N-terminal extension is rich in Asp residues,

545 suggesting that it could make transient interactions with the positively charged MAX
546 core in the absence of its cellular target. In MAX62 (AVR-Pib), a surface loop region
547 forms a strong positive patch (Fig 7C), which has been shown to be essential for the
548 avirulence function of AVR-Pib and its nuclear localization in host cells [35].
549 Interestingly, a similar positive patch is visible on the surface of its structural
550 homologs MAX61 belonging to the same structural group, as well as in MAX05 and
551 MAX72 belonging to group O (Table1), suggesting that these effectors may also rely
552 on this positive surface loop for their function. Similarly, AvrPiz-t displays a positively
553 charged surface partially involving lysine residues that are required for AvrPiz-t
554 avirulence and virulence functions in rice [14]. Inversely, while the surface of MAX86
555 (AVR1-CO39) is strongly negative, that of MAX93 (AVR-Pia) is neutral, yet both
556 AVR1-CO39 and AVR-Pia interact similarly through their β 2 strand with the HMA
557 domain from the rice immune receptors RGA5 [36] and Pikp-1 [37], respectively.



558

559 **Fig 7. Surface properties of the MAX core domains.**

560 Surface properties of MAX core domains computed and represented using SURFMAP. (A) Schematic
 561 of calculation of the spherical coordinates (from Schweke et al., 2022). The coordinates of each
 562 surface particle G_i is expressed in spherical coordinates (ρ, φ, θ) , where ρ represents the distance of
 563 the particle G_i to the center of mass G of the protein, φ is the angle between the X axis and the
 564 projected vector $\overrightarrow{GG_i}$ in the plan $(\overrightarrow{GX}, \overrightarrow{GY})$, while θ is the angle between the vector $\overrightarrow{GG_i}$ and the Z axis.

565 **B)** MoToxB structure showing the 6 β -strands of the MAX core with the color code used for the
566 surface representation in panel C. **C)** 2D maps of exposed β -strands, electrostatic potential and
567 stickiness of the molecular surfaces calculated by SURFMAP for MAX domains extracted from AF2
568 models of MAX effectors with known structure. N- and C-terminal extensions were discarded and the
569 MAX core 3D models were all superimposed to AF_MAX33 (MoToxB) giving a reference frame for the
570 Sanson-Flamsteed 2D projection computed surfaces. The β -strand maps use the color code given in
571 panel B, the electrostatic potential maps are scaled in the indicated kT/e units and the stickiness
572 (related to hydrophobicity) scale is that defined by Levy E. D., 2010 [38]. **D)** Comparison of overall
573 surface electrostatic potentials of MAX core domains, summed over the entire molecular surface and
574 normalized by the highest absolute value calculated for the subset of 49 MAX effector models (S2
575 files). **E)** Relative surface stickiness of MAX core β -strands. Stickiness values were summed for
576 residues forming each of the 6 β -strands of the MAX core domains and normalized by the highest
577 value calculated for each strand in the subset of 49 MAX core models.

578

579 Wide divergence is also observed in the surface stickiness of the MAX
580 domains. Surface stickiness is mostly related to surface hydrophobicity and reflects
581 the propensity of each amino acid to be involved in molecular interfaces [38]. For
582 AVR-Pia, the HMA binding site correlates well with the presence of a large
583 hydrophobic patch on the surface (Fig 7C and panel C in S5 Fig) and a very sticky β 2
584 strand, also present in MAX31 (Fig 7E). This is however not the case for AVR1-CO39
585 whose surface hydrophobicity is limited except in strand β 5. This strand is particularly
586 variable in length and surface properties, exhibiting high stickiness in only a few MAX
587 effectors (e.g. MAX10, MAX11 and MAX38) where it could contribute to the binding
588 site of host target proteins. For the AVR-Pik group (MAX01, MAX02 and MAX03)
589 surface stickiness is high in β 1 and sticky patches are also observed in strands β 3,
590 β 4 and β 6. In all these effectors, the β 3 stickiness could serve in an interaction with
591 strand β 4 of HMA domains, as observed in complexes of different MAX02 effectors
592 with the HMA domain from Pikp-1 or from the rice protein OsHIP19 targeted by
593 AVR-PikF [8–10]. Other MAX effectors (e.g. MAX67, MAX72 and MAX78) possess a
594 highly sticky β 3 strand that could also associate with the β -strand of an HMA domain

595 or other type of protein domain. In the crystal structures of the AVR-Pik effectors, the
596 anti-parallel β 1- β 6 strands of the MAX core are making hydrophobic contacts with
597 residues in their N-terminal extension which adopts a conserved extended
598 conformation and considerably expands the binding interface with the HMA (S5 Fig).
599 In MAX structural groups A to D of Table 1 (not included in the present subset), a
600 sticky β 6 strand often associates with an anti-parallel β 7 extending the MAX core β -
601 sheet. Similarly, the highly hydrophobic β 6 strand present in MAX33 (MoToxB),
602 MAX45 and MAX50 could interact with target proteins through an antiparallel β -
603 strand arrangement.

604 Altogether, this analysis highlights the very variegated surface properties
605 exhibited by the *P. oryzae* MAX effectors. In spite of sharing a common fold, these
606 sequence diverse proteins retain very high diversity at the structural level. On the
607 other hand, sequence conservation is high inside each OG cluster with average
608 conservation scores in strands and loops close to the maximum conservation score
609 of 9 (S7c Table). Three clusters display low conservation scores in β 2, β 3 and β 6
610 strands represented by MAX47, in β 2 and the loop joining β 4 to β 5 for MAX63, and
611 in strands β 4 and β 5 for MAX70, and accordingly, higher polymorphism on their
612 surfaces (S6 Fig and S2 Files).

613

614 Discussion

615 We initially used hybrid multiple template modeling that combines information
616 from multiple template structures to predict the core of MAX effector structures. The
617 best models were selected according to their predicted TM-score (TM-pred), a
618 commonly used measure to assess the structural similarity between predicted
619 models and the true native structure. By comparing new experimental MAX effector

620 NMR structures with their corresponding TM-pred models indicated the low accuracy
621 of the models, pointing to the limits of template-based homology modeling [39] and
622 the need of alternative modeling strategies to model MAX effectors.

623

624 *Ab initio modeling*

625 Recently, *ab initio* modeling, specifically using Rosetta and the two web
626 servers Robetta and QUARK, was applied for predicting the structures of already
627 known MAX effector proteins of *Magnaporthe oryzae* [40]. The Rosetta *ab initio*
628 modeling approach generated models with the best overall TM-scores, with AVR-Pib
629 achieving the highest TM-score. The exception to this trend was AVR-Pik, for which
630 the QUARK method produced the best model with a TM-score of 0.89, compared to a
631 TM-score of 0.51 in Rosetta. Overall, the study highlights the strengths and limitations
632 of *ab initio* modeling for predicting the structures of fungal effector proteins. While *ab*
633 *initio* methods can provide valuable insights into the overall fold and topology of
634 proteins, accurately predicting detailed secondary structures remains challenging,
635 especially in the cases where the TM-scores are relatively low. The performance of
636 different *ab initio* methods can also vary depending on the specific protein being
637 modeled. To address the issue of missing secondary structures or other structural
638 defects, further refinement techniques or hybrid methods can be employed. These
639 approaches aim to improve the accuracy of the predicted models by incorporating
640 additional information, such as experimental data, molecular dynamics simulations
641 [41], fragment assembly [42], or consensus modeling that can be used to refine and
642 improve the quality of predicted models. Although this can improve the robustness
643 and accuracy of the predicted models, it involves additional computational steps and
644 requires the availability of multiple predictions.

645 *Modeling of MAX effectors from M. oryzae strain 70-15 using deep learning*

646 TrRosetta and AlphaFold are novel computational methods based on deep
647 learning techniques to predict protein structures from amino acid sequences,
648 bypassing some of the computationally-intensive steps required by traditional
649 methods. The MAX family repertoire of *M. oryzae* strain 70-15 was investigated and
650 models were generated by computational methods mostly using TrRosetta [3] and
651 AlphaFold [4,5]. The first study (TrRosetta models) identified 11 MAX candidates and
652 similar population sizes of 26 and 32 MAX candidates were reported for the two other
653 AlphaFold studies, respectively. While 10 MAX of these candidate models were
654 commonly identified and systematically assigned to MAX effectors by all three
655 studies, another set of 22 MAX effectors were identified in less than three studies (S8
656 Table), indicating the difficulties in model selection based on pTM-score and in
657 detecting structural similarity using methods like CATH [43] and SCOPE [44].

658 Most of the MAX effectors that were previously reported in the TrRosetta and
659 AlphaFold studies were also identified in our analysis (Table 1 and S8 Table) with the
660 exception of OG54 that we did not select as a MAX effector. MAX members of the
661 groups C, E and H were not found in these previous reports while the equivalent
662 sequences in the *M. oryzae* strain 70-15 for MAX members of groups J and K could
663 not be found.

664 In our study we used the pLDDT score (predicted *Local Distance Difference*
665 *Test*), which provides a residue-level assessment of the confidence or accuracy of
666 each residue's predicted position in the protein structure. By focusing on the pLDDT
667 scores within the MAX folded region, we specifically evaluated the local accuracy of
668 the predicted structure within the MAX core domain. This localized scoring approach
669 enables a more focused evaluation and filtering of the protein structure predictions,

670 and allows identification and selection of the best models with higher accuracy and
671 reliability within the specific region of interest. By comparing the experimental results
672 from NMR with the corresponding AF models, we were able to assess the accuracy
673 and reliability of the AF predictions.

674

675 *Venturia inaequalis* MAX-like effectors

676 *V. inaequalis* is an ascomycete fungus, in the *Venturiaceae* family, responsible
677 for apple scab disease. Assessing models of *V. inaequalis* MAX-like effectors [45]
678 against the criteria we defined here to assign MAX effectors to subfamilies, revealed
679 that none of the models fitted into any of the MAX subfamilies. Indeed, *V.*
680 *inaequalis* MAX effectors present three remarkable disulfide bonds. One is the
681 canonical “1” bond found in other MAX effectors, while the remaining two were not
682 found in any of the MAX effectors from *P. oryzae*. Moreover, MAX-like effectors of *V.*
683 *inaequalis* usually possess a C-terminal helical extension connected to the MAX core
684 domain *via* a specific disulfide bond that was not observed in any MAX from *P.*
685 *oryzae*. This makes these newly discovered MAX-like effectors from *V. inaequalis*
686 another subfamily with unique sequence/structure features [45]. As *V.*
687 *inaequalis* exclusively colonizes and releases effectors in the subcuticular host
688 environment without penetrating the underlying epidermal cells, their function, and
689 thus targets, are probably fundamentally different from the other studied MAX
690 effectors from *P. oryzae*.

691

692 MAX effector AlphaFold models predicted in 120 *P. oryzae* genomes

693 Clustering of the 77 MAX effector models successfully predicted by AlphaFold
694 allowed us to distinguish 15 subfamilies. Our study showed that, beyond the well-

695 known conserved MAX core, the MAX superfamily is characterized by an important
696 structural diversity shown by additional structured regions in the C-terminal portions
697 of several of its members. Specifically, these include additional strands observed in
698 groups A to D and helical extensions observed in groups E to G. These regions may
699 play a role in protein-protein interactions or contribute to the effector's overall
700 functionality. On the other hand, long intrinsically disordered regions (IDRs) were
701 rarely observed in only six MAX effectors. IDR regions lack a stable 3D structure and
702 exhibit conformational flexibility, allowing them to interact with multiple binding
703 partners and fulfill various functions [46] but are difficult to predict from the sequence
704 [47].

705 Furthermore, the study also identified more modest structural variations within
706 the MAX core for seven groups, labeled from I to O. These variations indicate that
707 even within the core structural framework of the MAX effectors, there are subtle
708 differences that distinguish these groups from each other. The classification given in
709 Table 1 can be improved by incorporating surface properties. Thus, the AVR-Pib and
710 O groups could be agglomerated, since they are structurally similar and members of
711 the O group have electrostatic surfaces related to AVR-Pib.

712 Notably, our study uncovered a domain duplication event within one of the
713 MAX effector clusters (group H). Other dual-domain effectors have been described in
714 recent studies, i.e. the Fol dual-domain effectors (FOLD) [48] and effectors predicted
715 from *Puccinia graminis* [4]. The discovery of dual-domain effectors, including the
716 domain duplication found in one of the MAX effector cluster, adds to our
717 understanding of the diversity and complexity of effector proteins. These dual-domain
718 effectors likely have evolved to possess multiple functional domains that contribute to
719 their virulence or interaction with host plants.

720 *β1 and β6 surface stickiness of AVR-Pik effectors*

721 The AVR-Pik AF models display high surface stickiness on β1 and β6 strands
722 that could serve to anchor residues from the N-terminal extensions of these effectors
723 to their MAX core domains. While there are multiple experimental structures of AVR-
724 Pik in complex with HMA domains, whether the structure of the free AVR-Pik effector
725 differs when not in complex with an HMA domain remains an open question. In the
726 AF models of MAX01, MAX02 and MAX03, the first 10-residues at the N-terminus
727 are unstructured. These are followed by a stretch of 20 residues, which are well
728 defined according to their pLDDT scores but without regular secondary structure, and
729 which adopt the conformation observed when the AVR-Pik effectors are in complex
730 with an HMA domain. Alternative AF models computed with the *Custom* MSA
731 implementation that does not use PDB templates showed different conformations for
732 this stretch of 20 residues, from totally unstructured (MAX01) to helical tendency
733 (MAX02). Based on these AF calculations we could expect that when free, AVR-Pik
734 effectors have a N-terminal extension alternating between different conformations but
735 we cannot exclude that this extension, while not having canonical secondary
736 structures, could participate to the overall stability of the AVR-Pik effectors.
737 Truncation mutants may serve to validate this hypothesis, however mutations within
738 or truncations of *a priori* unfolded protein regions may have deleterious effects not
739 only on the structure stability, as shown for N-terminal truncations of AVR-PikD
740 (pages 87-88 in ref. [49]) but also and more specifically on the overall folding process
741 of the protein. Recently, we used HP-NMR (high Hydrostatic Pressure NMR) [50,51]
742 to study the folding/unfolding of AVR-Pia, AVR-Pib [52] and MAX60 [53]. In the case
743 of MAX60, we observed an early folding intermediate involving β1, β6 and the C-
744 terminal helix that is a specific extension of this MAX effector, and mutants lacking

745 this helix were not sufficiently stable to be purified. This demonstrates that the
746 presence or absence of additional sequences outside the core can have profound
747 impacts on the folding of these effectors.

748

749 *Concluding Remarks*

750 Beyond the scope of information derived from the primary sequence, structural
751 information expands our understanding of biological processes at the atomic level.
752 Moreover, the three-dimensional structures of the different partners can be indicative
753 of the evolutionary pressure exerted on a biological system. This is far to be trivial
754 especially in the case of sequence divergent effectors that are also found to form a
755 significant structural family. The presented prediction pipeline, associated with
756 modeling using AlphaFold already showed a successful prediction rate of MAX
757 effectors of nearly 80%. The quality of these results has been proven by the
758 experimental resolution of four new MAX effectors MAX28, MAX47, MAX60 and
759 MAX67, which revealed the outstanding accuracy of the predictions when
760 superimposed with their respective model, especially in the position and orientation
761 of the side chains and secondary structures. A subset of 20% of the OG cluster
762 sequences resulted in ambiguous models (unreliable or with major structural
763 deviation of the expected MAX fold) pointing out the limits of *de novo* prediction on
764 such divergent sequences. This emphasizes the significance of the experimental
765 structural elucidation, which remains the key evidence even if known to be
766 challenging and resource consuming. Nonetheless, structure modeling will provide
767 solid foundations for the structure characterization or the study of interacting
768 biological entities, when limited or no information at all is available. The surface
769 stickiness mapping while not unambiguously informing of what could be the protein

770 interface on the MAX domain surface, which is in contact with the host target, may
771 help to build hypothesis and to design plant biology experiments for validation.
772 Linked to these predictive studies of interfaces between MAX effectors and their
773 targets are new developments in Alphafold2, such as improved prediction of protein-
774 protein interactions [54] or screening of interactions between proteins [55].

775

776 The MAX family effector proteins provide an example where the core structural
777 platform has the plasticity to adapt extensions constituting new potential interacting
778 modules with target proteins. This structural variability within effector families is
779 important for their functional diversity and adaptability. By adding extensions or new
780 modules, effectors can acquire novel functionalities, interact with different host
781 targets, or modulate different host immune responses.

782

783 **Materials and Methods**

784 ***Experimental Structures***

785 *MAX28 Protein expression and purification.*

786 Protein expression and purification experimental details for MAX47, MAX60
787 and MAX67 are available in [56] Lahfa et al. 2022. For MAX28 we followed
788 essentially the same protocol than for the other MAX effectors for producing the ¹⁵N-
789 labelled NMR sample but the His₆-tag was not cleaved to keep the protein soluble.
790 Uniformly labeled ¹⁵N MAX28 was expressed in E. coli BL21 (DE3) cells (Invitrogen,
791 Thermo Fisher Scientific, Waltham, USA) from a homemade plasmid pDB-his-CCDB-
792 3C (courtesy of Frederic Allemand, CBS Montpellier, France). Protein expression
793 was carried out in ¹⁵NH₄Cl (1 g/l) enriched M9 medium. Cells were grown at 37 °C
794 until reaching an OD600 = 0.8 and then, expression proceeded overnight at 30 °C
795 after induction by addition of 0.3 mM IPTG. Cells were harvested by centrifugation,
796 re-suspended in denaturing buffer (50 mM Tris, 300 mM NaCl, 1 mM DTT
797 (dithiothreitol), 8 M urea, pH 8) and lysed by ultra-sonication. The supernatant
798 containing the unfolded protein was applied to a HisTrap HP 5 ml affinity column
799 (Cytiva, Freiburg im Breisgau, Germany). The His₆-tagged protein was eluted in 50
800 mM Tris, 300 mM NaCl, 1 mM DTT, 8 M urea, pH 8 with an imidazole gradient up to
801 500 mM. At this step, MAX28 was directly dialyzed against 10 mM Na Phosphate, 2
802 mM DTT, 150 mM NaCl, pH 6.8 buffer in order to remove imidazole and urea,
803 allowing the refolding of the protein. The MAX28 samples were then concentrated
804 using Amicon Ultra Centrifugal Filter Devices (MW cutoff 3000 Da), (Merck Millipore,
805 Burlington, USA) prior to size exclusion chromatography (SEC) using HiLoad 16/600
806 Superdex 75 pg column (Cytiva). Fractions containing protein were pooled,
807 concentrated to 0.4 mM and stored at -20°C. All NMR experiments were carried out

808 at 27°C on a Bruker Avance III 800 MHz or Bruker Avance III 700 MHz spectrometer,
809 both equipped with 5 mm z-gradient TCI cryoprobe. NMR samples consisted on
810 approximately 0.4 mM ¹⁵N-labeled protein dissolved in 10 mM Na-Phosphate buffer
811 (pH 6.8) and 150 mM NaCl with 5% D₂O for the lock.

812

813 *NMR Structure determination of MAX28, MAX47, MAX60 and MAX67.*

814 ¹H chemical shifts were directly referenced to the methyl resonance of DSS, while
815 ¹⁵N chemical shifts were referenced indirectly to the absolute ¹⁵N/¹H frequency ratio.
816 All NMR spectra were processed with Topspin 3.6 (Bruker) and analyzed with Cindy
817 2.1 (Padilla, www.cbs.cnrs.fr). Assignments for MAX28, MAX47, MAX60 and MAX67
818 have been deposited to and are available from the BMRB data bank under the
819 accession entry 34782, 34731, 34730 and 34729, respectively.

820 The NMR structures were determined from the NMR constraints listed in S4 Table
821 that were obtained as follow. NOE cross-peaks identified on 3D [¹H, ¹⁵N] NOESY-
822 HSQC (mixing time 150 ms) were assigned through automated NMR structure
823 calculations with CYANA3 [57,58]. Hydrogen bond restraints were derived using
824 standard criteria on the basis of the amide ¹H / ²H exchange experiments and NOE
825 data. When identified, the hydrogen bond was enforced using the following restraints:
826 ranges of 1.8–2.0 Å for d(N-H,O), and 2.7–3.0 Å for d(N,O). Dihedral restraints were
827 obtained from TALOS-N [59] analysis of backbone atom chemical shifts for MAX47,
828 MAX60 and MAX67. For the final list of restraints, distance values redundant with
829 covalent geometry were eliminated and disulfide bonds that were consistent with
830 short distances between cysteine residues were added.

831 A total of 200 three-dimensional structures were generated using the torsion angle
832 dynamics protocol of CYANA3 from NOEs, hydrogen bonds and disulfide bond

833 restraints (S4 Table). The 20 best structures (based on the final target penalty
834 function values) were minimized with CNS 1.2 according to the RECOORD procedure
835 [60] and analyzed with PROCHECK [61]. The rmsds were calculated with MOLMOL
836 [62]. All statistics are given in S4 Table.

837 The structure coordinates have been deposited at the Protein Data Bank under the
838 following accession codes: MAX28 (PDB_8C8A), MAX47 (PDB_7ZKD), MAX60
839 (PDB_7ZK0), MAX67 (PDB_7ZJY),).

840

841 ***TM-pred MAX models Web Table***

842 Homology models of each OG representative sequence relative to each 3D
843 template were built using MODELLER v9.1 [63] with several alternative query-template
844 threading alignments as described in [7]. The top-5 models were selected according
845 to the TM-pred scoring function and are given in
846 <https://pat.cbs.cnrs.fr/magmax/model/> Web page.

847 The Web table has the following columns: Group (OG cluster), Score (composite
848 evaluation score of the best model -best scores are in red, worst are in blue-), Dfire,
849 Goap, Qmean, E1D, E2D, E3D (individual evaluation scores of the best model),
850 Alignment (aligned identifier sequences), Identifier (protein identifier of the orthologs
851 prioritizing *Oryzae* infecting strains). Structural models and alignments are available
852 by clicking on each OG cluster in the first column. A multiple sequence alignment of
853 non-redundant orthologous proteins is displayed at the top of the page, starting with
854 the modeled representative sequence. For each OG cluster given in [7] we further
855 filtered out redundant sequences using CD-HIT [64] (S1 Table). The representative
856 sequence of each OG cluster was determined to be the sequence sharing the
857 highest sequence identity with a consensus sequence derived from the OG cluster

858 sequence alignment by MAFFT [65] (S2 Table). Signal peptide prediction before the
859 cleaved residue (cs.SIGNALP41), mean hydrophobic index (ih.MEAN), sequence
860 conservation (1D.CSRV), alternative alignments and model secondary structures
861 (2d.STRIDE) are displayed below the sequence alignment. Sequence conservation
862 scoring implemented in PAT [66] was calculated according to Sonnhammer and
863 Hollich, 2005 [67] with a Gonnet matrix [68]. At the bottom of the page, the 5 best
864 models can be displayed using different representations and color schemes. Models
865 can also be downloaded in PDB format.

866

867 ***Modeling by AlphaFold.***

868 For each OG representative sequence we computed three AF models differing
869 by the way of building multiple sequence alignment (MSA). The MMseqs2 MSA was
870 obtained from the MMseqs2 [69,70] web server as implemented in the ColabFold
871 version of AlphaFold 2.0 [71]. We also used the version of AlphaFold 2.2.0 that builds
872 MSAs by Jackhmmer on uniclust, mgnify and uniref90 databases. These two
873 implementations use PDB templates. Finally, a *Custom* MSA was build from
874 Muscle_v3.8.31 [72] by inserting (-profile option) the query sequence on top of a
875 previously computed MSA, termed $\beta 1\beta 4$ _MSA. The $\beta 1\beta 4$ _MSA was build from a
876 Muscle alignment of the OG sequences (S1 Table) by filtering out those having the
877 two flanking cysteine residues in the $\beta 1$ and in the loop between $\beta 4$ and $\beta 5$ strands
878 not correctly aligned to the 8 3D template sequences. The $\beta 1\beta 4$ _MSA was further
879 processed by truncating the sequences by eliminating residues (-2 included) before
880 and (+2 included) after the first and last aligned cysteine residues, respectively, and
881 filtering out for redundant sequences by CD-HIT, giving a total size of 247 aligned
882 sequences (S6 Table). For each query, the consistency of the *Custom* MSA was

883 determined by checking the correct alignment of the cysteine residues in the query
884 and in the appended $\beta 1\beta 4$ _MSA. When consistent the *Custom* MSA was converted
885 to a3m format by the reformat.pl script [73] and directly used as input in the
886 ColabFold implementation of AlphaFold 2.0 calculations that was setup without the
887 use of PDB templates. *Custom* MSAs could not be built for OG61 and OG62 from
888 absence of cysteine residues in their primary sequences and were not consistent for
889 OG15, OG27, OG71, OG81, OG85 and OG92.

890 The quality of each model was assessed by the pLDDT overall score [74]. The
891 correct MAX topology was verified by visual inspection (Pymol v.1.6 Delano 2002).
892 For models having the MAX topology, a MAX pLDDT score that was an average
893 score of residues in the MAX core domain (including residues from $\beta 1$ to $\beta 6$) was
894 calculated. For each query, the best AF MAX model was selected when the MAX
895 pLDDT score was above 60.

896

897 ***Dali implementation and search***

898 A standalone implementation of DaliLite.v5 [75] was used for this work. For the
899 all-to-all clustering by Dali we first discarded *unstructured* stretches in each model.
900 For this, the *structured* domain of each model was defined by taking the STRIDE [76]
901 output, and filtering for the first residue in the first and last residue in the last
902 secondary structure (helix or strand), respectively (S7 Table). The model of MAX52
903 was split in two chains A and B each containing a MAX domain. All these *structured*
904 domains were used for clustering with Dali Z-scores excluding *de-facto* unresolved
905 protein regions without losing important structural information.

906 *TM-align scoring and side-by-side plot with Dali Z-score tree.*

907 The distance between each pair of AF models that were used for Dali
908 clustering was estimated by the TM-score obtained from TM-align after pairwise
909 model superposition. A classification tree was then inferred from these pairwise
910 distances using FastME [77]. Finally, Fig 6 was obtained by joining identical models
911 in the FastME tree and in the Dali tree, respectively, by a line of the same color.

912

913 ***Surface properties of MAX core domains.***

914 A subset of 49 MAX effector AF models, each consisting of a MAX core
915 domain and optional N- and/or C- *unstructured* extensions (S7 Table) was defined by
916 discarding AF models having N- and/or C-terminal *structured* extensions (listed in the
917 groups A to H in Table 1 and in S4 Fig). All MAX core domains of the 49 AF models
918 were superimposed to the reference MoToxB structure with their β 1 strand vertically
919 aligned to the Z Cartesian axe giving a reference frame for the Sanson-Flamsteed 2D
920 projection computed using SURFMAP [31]. Their surface properties including
921 stickiness and electrostatics (APBS) [78] were computed by SURFMAP and are given
922 in S2 File. The temperature factor column of the PDB files was used to encode the
923 color of the exposed surface of the six β -strands, from 1 to 6, respectively. The sum
924 of the surface stickiness positive values of each individual β -strand was computed by
925 filtering SURFMAP surface stickiness output and are reported in Fig 7D. The amino-
926 acid conservation scores given for each OG cluster to which belongs each
927 representative MAX model were used to color encode the surface from white for high
928 conservation score of 9, light blue colors for intermediate conservation scores (from 8
929 to 6), sky-blue for low conservation score of 5 and darker blue colors indicating highly
930 polymorphic positions with conservation scores of 4 and below.

931

932

933

934 **Author Contributions:** M.L., and K.d.G. prepared the ^{15}N - ^{13}C -labeled protein
935 samples (sub-cloning, protein expression and purification). P.B. made the NMR
936 resonance assignment of the four proteins in the study conditions. J.G. wrote scripts
937 for protein sequence analysis and homology modeling. C.R. and A.P. supervised the
938 project, conceived experiments and modeling, participated in the interpretation, and
939 M.L., A.P., N.D., C.R., S.C., P.G. wrote the article. A.P. also contributed to the
940 funding acquisition with P.G. and T.K. All authors have read and agreed to the
941 published version of the manuscript.

942

943 **Funding:** This research project was funded by the ANR project MagMAX (ANR-18-
944 CE20-0016-02), the European Research Council (ERC-2019-STG-852482-ii-MAX),
945 and supported by French Infrastructure for Integrated Structural Biology (FRISBI)
946 grant No. ANR-10-INSB-05.

947

948 **Acknowledgements**

949 We are grateful to Liisa Holm for feedback in implementing Dali. The authors
950 are grateful to J. Maidment (CBS, Montpellier) for careful proof reading and language
951 correction of our manuscript. We are grateful to Matthew Bowler and Didier Nurizzo
952 at the European Synchrotron Radiation Facility (ESRF), Grenoble, France for
953 providing assistance in using beamline ID30A-1. The authors gratefully acknowledge
954 the ESRF for provision of synchrotron radiation facilities via Block Allocation Group
955 beamtime.

956

957

958 **Supporting information**

959 S1 Fig. Template-based modeling of MAX effector sequences

960 S2 Fig. NMR structures and AF models

961 S3 Fig. Groups of AlphaFold models

962 S4 Fig. Singletons MAX effectors with structured extensions

963 S5 Fig. Hydrophobic residues on the surface of AVR-Pik and AVR-Pia

964 S6 Fig. Amino-acid polymorphism mapped on the surface of AF MAX models

965 S1 Table. List of *Pyricularia* (syn. *Magnaporthe*) *oryzae* entries in the 94 MAX
966 effector orthogroup (OG) clusters

967 S2 Table. Representative sequences of the 94 MAX effector orthogroup clusters

968 S3 Table. Report on structural studies of 10 putative MAX effectors (OG proteins)

969 S4 Table. Refinement statistics of MAX effector NMR structures and AF model
970 superimposition

971 S5 Table. Summary of AlphaFold2 modeling statistics and list of validated MAX
972 effectors

973 S6 Table. $\beta 1\beta 4$ MSA

974 S7 Table. Structural features of 77 AF-modeled structures of validated MAX effector,
975 statistics and conservation scores.

976 S8 Table. Comparizon of our selection of MAX effectors with previous modelisation
977 studies

978 Supplementary Materials_and_Methods. Crystallographic structure determination of
979 MoToxB

980 S1 File. Zipped folder of AF MAX models

981 S2 File. Zipped folder of AF MAX models surfaces

982

983

984 **References**

- 985 1. Lo Presti L, Lanver D, Schweizer G, Tanaka S, Liang L, Tollot M, et al. Fungal
986 Effectors and Plant Susceptibility. *Annu Rev Plant Biol.* 2015;66: 513–545.
987 doi:10.1146/annurev-arplant-043014-114623
- 988 2. Sperschneider J, Williams AH, Hane JK, Singh KB, Taylor JM. Evaluation of
989 Secretion Prediction Highlights Differing Approaches Needed for Oomycete and Fungal
990 Effectors. *Front Plant Sci.* 2015;6. doi:10.3389/fpls.2015.01168
- 991 3. Seong K, Krasileva KV. Computational Structural Genomics Unravels Common
992 Folds and Novel Families in the Secretome of Fungal Phytopathogen *Magnaporthe*
993 *oryzae*. *Mol Plant-Microbe Interactions®.* 2021;34: 1267–1280. doi:10.1094/MPMI-03-
994 21-0071-R
- 995 4. Seong K, Krasileva KV. Prediction of effector protein structures from fungal
996 phytopathogens enables evolutionary analyses. *Nat Microbiol.* 2023;8: 174–187.
997 doi:10.1038/s41564-022-01287-6
- 998 5. Yan X, Tang B, Ryder LS, MacLean D, Were VM, Eseola Bisola A, et al. The
999 transcriptional landscape of plant infection by the rice blast fungus *Magnaporthe oryzae*
1000 reveals distinct families of temporally co-regulated and structurally conserved effectors.
1001 *Plant Cell.* 2023;35: 1360–1385. doi:<https://doi.org/10.1093/plcell/koad036>
- 1002 6. de Guillen K, Ortiz-Vallejo D, Gracy J, Fournier E, Kroj T, Padilla A. Structure
1003 Analysis Uncovers a Highly Diverse but Structurally Conserved Effector Family in
1004 Phytopathogenic Fungi. *PLOS Pathog.* 2015;11: e1005228.
- 1005 7. Le Naour—Vernet M, Charriat F, Gracy J, Cros-Arteil S, Ravel S, Veillet F, et al.
1006 Adaptive evolution in virulence effectors of the rice blast fungus *Pyricularia oryzae*. Seidl
1007 MF, editor. *PLOS Pathog.* 2023;19: e1011294. doi:10.1371/journal.ppat.1011294
- 1008 8. Maqbool A, Saitoh H, Franceschetti M, Stevenson CEM, Uemura A, Kanzaki H, et al.
1009 Structural basis of pathogen recognition by an integrated HMA domain in a plant NLR
1010 immune receptor. *eLife.* 2015;4: e08709.
- 1011 9. De la Concepcion JC, Franceschetti M, Maqbool A, Saitoh H, Terauchi R, Kamoun S,
1012 et al. Polymorphic residues in rice NLRs expand binding and response to effectors of the
1013 blast pathogen. *Nat Plants.* 2018 [cited 10 Jul 2018]. doi:10.1038/s41477-018-0194-x
- 1014 10. Maidment JHR, Franceschetti M, Maqbool A, Saitoh H, Jantasuriyarat C, Kamoun S,
1015 et al. Multiple variants of the fungal effector AVR-Pik bind the HMA domain of the rice
1016 protein OsHIPP19, providing a foundation to engineer plant defense. *J Biol Chem.*
1017 2021;296: 100371. doi:10.1016/j.jbc.2021.100371
- 1018 11. Zhang S, Wang L, Wu W, He L, Yang X, Pan Q. Function and evolution of
1019 *Magnaporthe oryzae* avirulence gene *AvrPib* responding to the rice blast resistance gene
1020 *Pib*. *Sci Rep.* 2015;5: 11642. doi:10.1038/srep11642
- 1021 12. Oikawa K, Fujisaki K, Shimizu M, Takeda T, Saitoh H, Hirabuchi A, et al. The blast
1022 pathogen effector AVR-Pik binds and stabilizes rice heavy metal-associated (HMA)
1023 proteins to co-opt their function in immunity. *Plant Biology*; 2020 Dec.
1024 doi:10.1101/2020.12.01.406389
- 1025 13. Park CH, Shirsekar G, Bellizzi M, Chen S, Songkumarn P, Xie X, et al. The E3 Ligase
1026 APIP10 Connects the Effector *AvrPiz-t* to the NLR Receptor *Piz-t* in Rice. Dinesh-Kumar
1027 SP, editor. *PLOS Pathog.* 2016;12: e1005529. doi:10.1371/journal.ppat.1005529
- 1028 14. Bai P, Park C, Shirsekar G, Songkumarn P, Bellizzi M, Wang G. Role of lysine
1029 residues of the *Magnaporthe oryzae* effector *AvrPiz-t* in effector- and PAMP-triggered
1030 immunity. *Mol Plant Pathol.* 2019;20: 599–608. doi:10.1111/mpp.12779
- 1031 15. Xu J, Zhang Y. How significant is a protein structure similarity with TM-score =

- 1032 0.5? *Bioinformatics*. 2010;26: 889–895. doi:10.1093/bioinformatics/btq066
- 1033 16. Jumper J, Evans R, Pritzel A, Green T, Figurnov M, Ronneberger O, et al. Highly
1034 accurate protein structure prediction with AlphaFold. *Nature*. 2021;596: 583–589.
1035 doi:10.1038/s41586-021-03819-2
- 1036 17. Senior AW, Evans R, Jumper J, Kirkpatrick J, Sifre L, Green T, et al. Improved
1037 protein structure prediction using potentials from deep learning. *Nature*. 2020;577:
1038 706–710. doi:10.1038/s41586-019-1923-7
- 1039 18. Taylor WR. Residual colours: a proposal for aminochromography. *Protein Eng*
1040 *Des Sel*. 1997;10: 743–746. doi:10.1093/protein/10.7.743
- 1041 19. Källberg M, Wang H, Wang S, Peng J, Wang Z, Lu H, et al. Template-based protein
1042 structure modeling using the RaptorX web server. *Nat Protoc*. 2012;7: 1511–1522.
1043 doi:10.1038/nprot.2012.085
- 1044 20. Baek M, DiMaio F, Anishchenko I, Dauparas J, Ovchinnikov S, Lee GR, et al.
1045 Accurate prediction of protein structures and interactions using a three-track neural
1046 network. *Science*. 2021;373: 871–876. doi:10.1126/science.abj8754
- 1047 21. Van Der Lee R, Buljan M, Lang B, Weatheritt RJ, Daughdrill GW, Dunker AK, et al.
1048 Classification of Intrinsically Disordered Regions and Proteins. *Chem Rev*. 2014;114:
1049 6589–6631. doi:10.1021/cr400525m
- 1050 22. Liu Y, Chen S, Wang X, Liu B. Identification of Intrinsically Disordered Proteins
1051 and Regions by Length-Dependent Predictors Based on Conditional Random Fields. *Mol*
1052 *Ther - Nucleic Acids*. 2019;17: 396–404. doi:10.1016/j.omtn.2019.06.004
- 1053 23. Monzon AM, Necci M, Quaglia F, Walsh I, Zanotti G, Piovesan D, et al.
1054 Experimentally Determined Long Intrinsically Disordered Protein Regions Are Now
1055 Abundant in the Protein Data Bank. *Int J Mol Sci*. 2020;21: 4496.
1056 doi:10.3390/ijms21124496
- 1057 24. Marín M, Uversky VN, Ott T. Intrinsic Disorder in Pathogen Effectors: Protein
1058 Flexibility as an Evolutionary Hallmark in a Molecular Arms Race. *Plant Cell*. 2013;25:
1059 3153–3157. doi:10.1105/tpc.113.116319
- 1060 25. Sun H, Zhu X, Li C, Ma Z, Han X, Luo Y, et al. *Xanthomonas* effector XopR hijacks
1061 host actin cytoskeleton via complex coacervation. *Nat Commun*. 2021;12: 4064.
1062 doi:10.1038/s41467-021-24375-3
- 1063 26. Aparicio Chacón MV, Van Dingenen J, Goormachtig S. Characterization of
1064 Arbuscular Mycorrhizal Effector Proteins. *Int J Mol Sci*. 2023;24: 9125.
1065 doi:10.3390/ijms24119125
- 1066 27. Jaswal R, Rajarammohan S, Dubey H, Kiran K, Rawal H, Sonah H, et al. Intrinsically
1067 Disordered Kiwellin Protein-Like Effectors Target Plant Chloroplasts and are
1068 Extensively Present in Rust Fungi. *Mol Biotechnol*. 2023.
1069 doi:https://doi.org/10.1007/s12033-023-00717-y
- 1070 28. Walsh I, Martin AJM, Di Domenico T, Tosatto SCE. ESpritz: accurate and fast
1071 prediction of protein disorder. *Bioinformatics*. 2012;28: 503–509.
1072 doi:10.1093/bioinformatics/btr682
- 1073 29. Holm L. DALI and the persistence of protein shape. *Protein Sci*. 2020;29: 128–
1074 140. doi:10.1002/pro.3749
- 1075 30. Zhang Y, Skolnick J. TM-align: a protein structure alignment algorithm based on
1076 the TM-score. *Nucleic Acids Res*. 2005;33: 2302–2309. doi:10.1093/nar/gki524
- 1077 31. Schweke H, Mucchielli M-H, Chevrollier N, Gosset S, Lopes A. SURFMAP: A
1078 Software for Mapping in Two Dimensions Protein Surface Features. *J Chem Inf Model*.
1079 2022;62: 1595–1601. doi:10.1021/acs.jcim.1c01269
- 1080 32. Giraldo MC, Valent B. Filamentous plant pathogen effectors in action. *Nat Rev*

- 1081 Microbiol. 2013;11: 800–814. doi:10.1038/nrmicro3119
1082 33. Wang H, Chou C, Hsu K, Lee C, Wang AH -J. New paradigm of functional regulation
1083 by DNA mimic proteins: Recent updates. IUBMB Life. 2019;71: 539–548.
1084 doi:10.1002/iub.1992
1085 34. Dennehy R, Duggan N, Dignam S, McCormack S, Dillon E, Molony J, et al. Protein
1086 with negative surface charge distribution, Bnr1, shows characteristics of a DNA-mimic
1087 protein and may be involved in the adaptation of *Burkholderia cenocepacia*.
1088 MicrobiologyOpen. 2022;11. doi:10.1002/mbo3.1264
1089 35. Goldenberg NM, Steinberg BE. Surface Charge: A Key Determinant of Protein
1090 Localization and Function. Cancer Res. 2010;70: 1277–1280. doi:10.1158/0008-
1091 5472.CAN-09-2905
1092 36. Guo L, Zhang Y, Ma M, Liu Q, Zhang Y, Peng Y, et al. Crystallization of the rice
1093 immune receptor RGA5A_S with the rice blast fungus effector AVR1-CO39 prepared *via*
1094 mixture and tandem strategies. Acta Crystallogr Sect F Struct Biol Commun. 2018;74:
1095 262–267. doi:10.1107/S2053230X18003618
1096 37. Varden FA, Saitoh H, Yoshino K, Franceschetti M, Kamoun S, Terauchi R, et al.
1097 Cross-reactivity of a rice NLR immune receptor to distinct effectors from the rice blast
1098 pathogen *Magnaporthe oryzae* provides partial disease resistance. J Biol Chem.
1099 2019;294: 13006–13016. doi:10.1074/jbc.RA119.007730
1100 38. Levy ED. A Simple Definition of Structural Regions in Proteins and Its Use in
1101 Analyzing Interface Evolution. J Mol Biol. 2010;403: 660–670.
1102 doi:10.1016/j.jmb.2010.09.028
1103 39. Fiser A. Template-Based Protein Structure Modeling. In: Fenyő D, editor.
1104 Computational Biology. Totowa, NJ: Humana Press; 2010. pp. 73–94. doi:10.1007/978-
1105 1-60761-842-3_6
1106 40. Rozano L, Mukuka YM, Hane JK, Mancera RL. Ab Initio Modelling of the Structure
1107 of ToxA-like and MAX Fungal Effector Proteins. Int J Mol Sci. 2023;24: 6262.
1108 doi:10.3390/ijms24076262
1109 41. Radom F, Plückthun A, Paci E. Assessment of ab initio models of protein
1110 complexes by molecular dynamics. MacKerell A, editor. PLOS Comput Biol. 2018;14:
1111 e1006182. doi:10.1371/journal.pcbi.1006182
1112 42. Mortuza SM, Zheng W, Zhang C, Li Y, Pearce R, Zhang Y. Improving fragment-
1113 based ab initio protein structure assembly using low-accuracy contact-map predictions.
1114 Nat Commun. 2021;12: 5011. doi:10.1038/s41467-021-25316-w
1115 43. Sillitoe I, Dawson N, Lewis TE, Das S, Lees JG, Ashford P, et al. CATH: expanding
1116 the horizons of structure-based functional annotations for genome sequences. Nucleic
1117 Acids Res. 2019;47: D280–D284. doi:10.1093/nar/gky1097
1118 44. Fox NK, Brenner SE, Chandonia J-M. SCOPe: Structural Classification of Proteins—
1119 extended, integrating SCOP and ASTRAL data and classification of new structures.
1120 Nucleic Acids Res. 2014;42: D304–D309. doi:10.1093/nar/gkt1240
1121 45. Rocafort M, Bowen JK, Hassing B, Cox MP, McGreal B, de la Rosa S, et al. The
1122 *Venturia inaequalis* effector repertoire is dominated by expanded families with
1123 predicted structural similarity, but unrelated sequence, to avirulence proteins from
1124 other plant-pathogenic fungi. BMC Biol. 2022;20: 246. doi:10.1186/s12915-022-01442-
1125 9
1126 46. Bondos SE, Dunker AK, Uversky VN. On the roles of intrinsically disordered
1127 proteins and regions in cell communication and signaling. Cell Commun Signal. 2021;19:
1128 88, s12964-021-00774–3. doi:10.1186/s12964-021-00774-3
1129 47. Zhao B, Kurgan L. Deep learning in prediction of intrinsic disorder in proteins.

- 1130 Comput Struct Biotechnol J. 2022;20: 1286–1294. doi:10.1016/j.csbj.2022.03.003
1131 48. Yu DS, Outram MA, Smith A, McCombe CL, Khambalkar PB, Rima SA, et al. The
1132 structural repertoire of *Fusarium oxysporum* f. sp. *lycopersici* effectors revealed by
1133 experimental and computational studies. biorxiv; 2021 Dec.
1134 doi:10.1101/2021.12.14.472499
- 1135 49. Varden FA. Structure/function studies of effectors from the potato late blight and
1136 rice blast pathogens. University of East Anglia. 2019. Available:
1137 [https://ueaeprints.uea.ac.uk/id/eprint/70234/1/FAVarden_100085474_PhD_Feb2019.](https://ueaeprints.uea.ac.uk/id/eprint/70234/1/FAVarden_100085474_PhD_Feb2019.pdf)
1138 pdf
- 1139 50. Dubois C, Herrada I, Barthe P, Roumestand C. Combining High-Pressure
1140 Perturbation with NMR Spectroscopy for a Structural and Dynamical Characterization of
1141 Protein Folding Pathways. *Molecules*. 2020;25: 5551. doi:10.3390/molecules25235551
- 1142 51. Roche J, Dellarole M, Royer CA, Roumestand C. Exploring the Protein Folding
1143 Pathway with High-Pressure NMR: Steady-State and Kinetics Studies. In: Akasaka K,
1144 Matsuki H, editors. *High Pressure Bioscience*. Dordrecht: Springer Netherlands; 2015.
1145 pp. 261–278. Available: http://link.springer.com/10.1007/978-94-017-9918-8_13
- 1146 52. Dubois C, Lahfa M, Pissarra J, de Guillen K, Barthe P, Kroj T, et al. Combining High-
1147 Pressure NMR and Geometrical Sampling to Obtain a Full Topological Description of
1148 Protein Folding Landscapes: Application to the Folding of Two MAX Effectors from
1149 *Magnaporthe oryzae*. *Int J Mol Sci*. 2022;23: 5461. doi:10.3390/ijms23105461
- 1150 53. Lahfa M, Mouhand A, de Guillen K, Barthe P, Kroj T, Roumestand C. Does a Similar
1151 3D Structure Mean a Similar Folding Pathway? The Presence of a C-Terminal α -Helical
1152 Extension in the 3D Structure of MAX60 Drastically Changes the Folding Pathway
1153 Described for Other MAX-Effectors from *Magnaporthe oryzae*. 2023.
- 1154 54. Bryant P, Pozzati G, Elofsson A. Improved prediction of protein-protein
1155 interactions using AlphaFold2. *Nat Commun*. 2022;13: 1265. doi:10.1038/s41467-022-
1156 28865-w
- 1157 55. Yu D, Chojnowski G, Rosenthal M, Kosinski J. AlphaPulldown—a python package
1158 for protein–protein interaction screens using AlphaFold-Multimer. Cowen L, editor.
1159 *Bioinformatics*. 2023;39: btac749. doi:10.1093/bioinformatics/btac749
- 1160 56. Lahfa M, Padilla A, De Guillen K, Pissarra J, Raji M, Cesari S, et al. 1H, 13C, 15 N
1161 backbone and side-chain NMR assignments for three MAX effectors from *Magnaporthe*
1162 *oryzae*. *Biomol NMR Assign*. 2022;16: 305–309. doi:10.1007/s12104-022-10095-2
- 1163 57. Güntert P. Automated NMR structure calculation with CYANA. *Methods Mol Biol*
1164 Clifton NJ. 2004;278: 353–378. doi:10.1385/1-59259-809-9:353
- 1165 58. Güntert P, Buchner L. Combined automated NOE assignment and structure
1166 calculation with CYANA. *J Biomol NMR*. 2015 [cited 18 Apr 2015]. doi:10.1007/s10858-
1167 015-9924-9
- 1168 59. Shen Y, Bax A. Protein Structural Information Derived from NMR Chemical Shift
1169 with the Neural Network Program TALOS-N. In: Cartwright H, editor. *Artificial Neural*
1170 *Networks*. New York, NY: Springer New York; 2015. pp. 17–32. doi:10.1007/978-1-
1171 4939-2239-0_2
- 1172 60. Nederveen AJ, Doreleijers JF, Vranken W, Miller Z, Spronk CAEM, Nabuurs SB, et
1173 al. RECOORD: A recalculated coordinate database of 500+ proteins from the PDB using
1174 restraints from the BioMagResBank. *Proteins Struct Funct Bioinforma*. 2005;59: 662–
1175 672. doi:10.1002/prot.20408
- 1176 61. Laskowski RA, MacArthur MW, Moss DS, Thornton JM. PROCHECK—a program to
1177 check the stereochemical quality of protein structures. : 283–291.
- 1178 62. Koradi R, Billeter M, Wüthrich K. MOLMOL: A program for display and analysis of

- 1179 macromolecular structures. *J Mol Graph*. 1996;14: 51–55.
- 1180 63. Webb B, Sali A. Protein Structure Modeling with MODELLER. *Methods Mol Biol*.
1181 2020;2199: 239–255. doi:10.1007/978-1-0716-0892-0_14
- 1182 64. Fu L, Niu B, Zhu Z, Wu S, Li W. CD-HIT: accelerated for clustering the next-
1183 generation sequencing data. *Bioinformatics*. 2012;28: 3150–3152.
1184 doi:10.1093/bioinformatics/bts565
- 1185 65. Katoh K, Standley DM. MAFFT Multiple Sequence Alignment Software Version 7:
1186 Improvements in Performance and Usability. *Mol Biol Evol*. 2013;30: 772–780.
1187 doi:10.1093/molbev/mst010
- 1188 66. Gracy J, Chiche L. PAT: a protein analysis toolkit for integrated biocomputing on
1189 the web. *Nucleic Acids Res*. 2005;33: W65–W71. doi:10.1093/nar/gki455
- 1190 67. Sonnhammer EL, Hollich V. Scoredist: A simple and robust protein sequence
1191 distance estimator. *BMC Bioinformatics*. 2005;6: 108. doi:10.1186/1471-2105-6-108
- 1192 68. Gonnet GH, Cohen MA, Brenner SA. Exhaustive Matching of the Entire Protein
1193 Sequence Database. *Science*. 1992;256: 1443–1445. doi:10.1126/science.1604319
- 1194 69. Steinegger M, Soding J. MMseqs2 enables sensitive protein sequence searching
1195 for the analysis of massive data sets. *Nat Biotechnol*. 2017;35: 1026–1028.
1196 doi:10.1038/nbt.3988
- 1197 70. Mirdita M, Steinegger M, Soding J. MMseqs2 desktop and local web server app for
1198 fast, interactive sequence searches. Hancock J, editor. *Bioinformatics*. 2019;35: 2856–
1199 2858. doi:10.1093/bioinformatics/bty1057
- 1200 71. Mirdita M, Schütze K, Moriwaki Y, Heo L, Ovchinnikov S, Steinegger M. ColabFold:
1201 making protein folding accessible to all. *Nat Methods*. 2022;19: 679–682.
1202 doi:10.1038/s41592-022-01488-1
- 1203 72. Edgar RC. MUSCLE: multiple sequence alignment with high accuracy and high
1204 throughput. *Nucleic Acids Res*. 2004;32: 1792–1797. doi:10.1093/nar/gkh340
- 1205 73. Remmert M, Biegert A, Hauser A, Soding J. HHblits: lightning-fast iterative protein
1206 sequence searching by HMM-HMM alignment. *Nat Methods*. 2011;9: 173–175.
1207 doi:10.1038/nmeth.1818
- 1208 74. Mariani V, Biasini M, Barbato A, Schwede T. IDDT: a local superposition-free score
1209 for comparing protein structures and models using distance difference tests.
1210 *Bioinformatics*. 2013;29: 2722–2728. doi:10.1093/bioinformatics/btt473
- 1211 75. Holm L. Using Dali for Protein Structure Comparison. In: Gáspári Z, editor.
1212 *Structural Bioinformatics*. New York, NY: Springer US; 2020. pp. 29–42.
1213 doi:10.1007/978-1-0716-0270-6_3
- 1214 76. Heinig M, Frishman D. STRIDE: a web server for secondary structure assignment
1215 from known atomic coordinates of proteins. *Nucleic Acids Res*. 2004;32: W500–W502.
1216 doi:10.1093/nar/gkh429
- 1217 77. Lefort V, Desper R, Gascuel O. FastME 2.0: A Comprehensive, Accurate, and Fast
1218 Distance-Based Phylogeny Inference Program: Table 1. *Mol Biol Evol*. 2015;32: 2798–
1219 2800. doi:10.1093/molbev/msv150
- 1220 78. Jurrus E, Engel D, Star K, Monson K, Brandi J, Felberg LE, et al. Improvements to
1221 the APBS biomolecular solvation software suite. *Protein Sci*. 2018;27: 112–128.
1222 doi:10.1002/pro.3280
- 1223